

Nebular Emission from Star-Forming Galaxies

Stéphane Charlot[★] and Marcella Longhetti[†]

Institut d’Astrophysique de Paris, CNRS, 98 bis Boulevard Arago, 75014 Paris, France

Accepted Received ... ; in original form ...

ABSTRACT

We present a new model for computing consistently the line and continuum emission from galaxies, based on a combination of recent population synthesis and photoionization codes. We use effective parameters to describe the H II regions and the diffuse gas ionized by single stellar generations in a galaxy, among which the most important ones are the zero-age effective ionization parameter, the effective gas metallicity, and the effective dust-to-heavy element ratio. We calibrate the nebular properties of our model using the observed [O III]/H β , [O II]/[O III], [S II]/H α , and [N II]/[S II] ratios of a representative sample of nearby spiral and irregular, starburst, and H II galaxies. To compute whole (line plus continuum) spectral energy distributions, we include the absorption by dust in the neutral interstellar medium (ISM) using a recent simple prescription, which is consistent with observations of nearby starburst galaxies. Our model enables us to interpret quantitatively the observed optical spectra of galaxies in terms of stars, gas, and dust parameters. We find that the range of ionized-gas properties spanned by nearby galaxies implies factors of 3.5 and 14 variations in the H α and [O II] luminosities produced per unit star formation rate (SFR). When accounting for stellar H α absorption and absorption by dust in the neutral ISM, the actual uncertainties in SFR estimates based on the emergent H α and [O II] luminosities are as high as several decades. We derive new estimators of the SFR, the gas-phase oxygen abundance, and the effective absorption optical depth of the dust in galaxies. We show that, with the help of other lines such as [O II], H β , [O III], [N II], or [S II], the uncertainties in SFR estimates based on H α can be reduced to a factor of only 2–3, even if the H α line is blended with the adjacent [N II] lines. Without H α , however, the SFR is difficult to estimate from the [O II], H β , and [O III] lines. The reason for this is that the absorption by dust in the neutral ISM and the ionized-gas parameters are then difficult to constrain independently. This suggests that, while insufficient by itself, the H α line is essential for estimating the star formation rate from the optical emission of a galaxy.

Key words: galaxies: general – galaxies: ISM – galaxies: stellar content.

1 INTRODUCTION

The most prominent tracers of star formation in the integrated spectra of galaxies are the emission lines produced by short-lived, massive stars. Several approximate formulae have been derived to convert the H α and [O II] luminosities of observed galaxies into star formation rates (SFRs; see the review by Kennicutt 1998). Calibrations of the H α luminosity emitted per unit SFR have consisted usually in applying

dust-free case B recombination to the stellar ionizing radiation predicted by a population synthesis model (e.g., Kennicutt 1983). The scaling of this luminosity by some empirical [O II]/H α ratio provides a calibration of the [O II] luminosity emitted per unit SFR (Gallagher, Hunter & Bushouse 1989; Kennicutt 1992b; see Barbaro & Poggianti 1997 for a more refined calibration). In reality, the absorption of ionizing photons by dust in H II regions could affect seriously the H α luminosity emerging from a star-forming galaxy (e.g., Mathis 1986b). Moreover, since the [O II]/H α ratio can vary by an order of magnitude in nearby star-forming galaxies, SFR estimates based on this ratio are subject to substantial uncertainties (Kennicutt 1998). To address these issues, we require a model for relating consistently the luminosities

[★] Currently on leave at the Max-Planck Institut für Astrophysik, Karl-Schwarzschild-Strasse 1, 85748 Garching, Germany

[†] Present address: Osservatorio Astronomico di Brera, Via Bianchi 46, 23807 Merate (LC), Italy

of emission lines to the stars, gas, and dust parameters of galaxies.

The optical-line ratios in the integrated spectra of nearby star-forming galaxies are similar to those in the spectra of individual H II regions (e.g., Lehnert & Heckman 1994; Kobulnicky, Kennicutt & Pizagno 1999). Photoionization models have proved essential to interpret the emission-line properties of H II regions in terms of stars and gas parameters (e.g., Evans & Dopita 1985). Thus, these models can potentially help us also interpret the nebular emission from galaxies in terms of macroscopic star formation parameters. In fact, photoionization models have already been combined with evolutionary population synthesis codes to constrain the ages and metallicities of giant extragalactic H II regions and H II galaxies (e.g., García-Vargas, Bressan & Díaz 1995, Stasińska & Leitherer 1996, and references therein). These studies, however, are not suited to spectral analyses of galaxies containing several stellar generations. Furthermore, until recently, combinations of photoionization and population synthesis models were limited by the lack of a simple prescription to compute consistently the effects of dust on the line and continuum emission from galaxies (see however Charlot & Fall 2000). It is now possible to build a model to interpret simultaneously the signatures of stars, gas, and dust in the integrated spectra of galaxies. The purpose of this paper is to present such a model.

We combine recent population synthesis and photoionization codes to compute the line and continuum emission from galaxies. We use effective parameters to describe the H II regions and the diffuse gas ionized by single stellar generations in a galaxy. We first calibrate the nebular properties of our model using the observed [O III]/H β , [O II]/[O III], [S II]/H α , and [N II]/[S II] ratios of a representative sample of nearby spiral and irregular, starburst, and H II galaxies. To compute whole (line plus continuum) spectral energy distributions, we then include the absorption by dust in the neutral interstellar medium (ISM) using a simple prescription, which is consistent with observations of nearby starburst galaxies (Charlot & Fall 2000). Our model succeeds in accounting quantitatively for the optical line and continuum emission from nearby star-forming galaxies of various types. Such spectral fits provide insights simultaneously into the star formation history, metallicity, and absorption by dust in the galaxies. This enables us to identify and calibrate new estimators of the star formation rate, the gas-phase oxygen abundance, and the effective absorption optical depth of the dust in galaxies.

We present our model in §2, where we express the nebular emission of a galaxy in terms of effective gas parameters. In §3, we compare our model with observations and identify the specific influence of each parameter on the integrated spectral properties of galaxies. In §4, we use the observed relations between various integrated spectral properties of nearby star-forming galaxies to construct estimators of the star formation rate, the gas-phase oxygen abundance, and the effective absorption optical depth of the dust. We express our results in terms of simple formulae derived for different assumptions about the available spectral information. Our conclusions are summarized in §5.

2 THE MODEL

In this section, we describe our model for the emission from stars and gas in galaxies. To begin with, in §2.1–2.3, we focus on the production of stellar radiation and its conversion into emission lines and recombination continuum by the gas. We compute the luminosity emerging from a galaxy in §2.4, where we include the absorption of photons emanating from the ionized regions by dust in the neutral (and molecular) ISM. We do not consider here the contribution to the ionizing radiation by active galactic nuclei (AGNs; see §4).

2.1 Basic Assumptions

The luminosity per unit wavelength $L_\lambda^+(t)$ produced at time t by the stars and the ionized gas in a galaxy can be expressed generally as

$$L_\lambda^+(t) = \int_0^t dt' \psi(t-t') S_\lambda(t') T_\lambda^+(t, t'). \quad (1)$$

Here $\psi(t-t')$ is the star formation rate at time $t-t'$, $S_\lambda(t')$ is the luminosity emitted per unit wavelength and per unit mass by a stellar generation of age t' , and $T_\lambda^+(t, t')$ is the ‘transmission function’ of the ionized gas, defined as the fraction of the radiation produced at wavelength λ at time t by a generation of stars of age t' that is transferred by the gas these stars ionize. Thus, $T_\lambda^+(t, t')$ must be regarded as the average transmission of the gas ionized by all stars of age t' within the galaxy. If the ionized regions are bounded by neutral material, $T_\lambda^+(t, t')$ will be close to zero at wavelengths blueward of the H-Lyman limit but greater than unity at the wavelengths corresponding to emission lines. To compute $L_\lambda^+(t)$ from equation (1), we make the following simplifying assumptions.

We neglect the ionization of the gas by hot intermediate- and low-mass stars; we thus write

$$T_\lambda^+(t, t') = 1, \quad \text{for } t' \geq t^{\text{OB}}, \quad (2)$$

where t^{OB} is the lifetime of massive stars producing most of the ionizing photons (§2.2). At ages greater than t^{OB} , planetary nebula nuclei are the dominant sources of ionizing photons in a single stellar generation. The ionizing radiation from planetary nebula nuclei, however, is typically less than 0.1 per cent of that produced at earlier ages by massive stars, even for initial mass functions (IMFs) with steep slopes and low upper cutoff masses (e.g., Charlot & Fall 1993; Binette et al. 1994). Since we are interested in galaxies in the process of forming massive stars, we therefore neglect the influence of the radiation from old planetary nebula nuclei on the gas.

We also neglect the influence of stellar winds and supernovae on the emission from galaxies. This is justified by both models and observations of star-forming galaxies. Leitherer & Heckman (1995) have computed the power injected into the ISM by stellar winds and supernovae for stellar populations with various IMFs and star formation histories. For a normal IMF, this amounts to less than 10 per cent of the power of the ionizing radiation from massive stars (see Fig. 69 of Leitherer & Heckman 1995). Observations support these results. About 20 to 50 per cent of the H-Balmer line emission from nearby spiral and irregular galaxies arises from ‘diffuse ionized gas’, which is not directly associated to individual H II regions (e.g., Hunter & Gallagher 1990;

Hoopes, Walterbos & Greenwalt 1996; Ferguson et al. 1996; Martin 1997). This gas, however, appears to also be heated primarily by the ionizing radiation from massive stars rather than by shocks (Mathis 1986a; Hunter & Gallagher 1990; Hoopes et al. 1996; Martin 1997; Wang, Heckman & Lehnert 1997). Direct evidence that 20 to 50 per cent of the ionizing photons produced in individual H II regions might leak into the ambient ISM further supports this result (Oey & Kennicutt 1997). Hence, for most purposes, the influence of stellar winds and supernovae on the nebular emission from galaxies can probably be neglected.

Finally, we assume for simplicity that the transmission function of the ionized gas depends only on the age t' of the stars producing the ionizing radiation, i.e.

$$T_\lambda^+(t, t') = T_\lambda^+(t'), \quad \text{for } t' < t^{\text{OB}}. \quad (3)$$

This approximation is adequate for the purpose of interpreting observations of star-forming galaxies. In fact, since the nebular emission depends only on the current gas content of the galaxies, specifying the dependence of T_λ^+ on the galaxy age t would involve arbitrary assumptions about the chemical enrichment history. We now appeal to standard codes to compute the radiation $S_\lambda(t')$ from the stars and the transmission function $T_\lambda^+(t')$ of the gas in our model.

2.2 Stellar Radiation

We compute the luminosity $S_\lambda(t')$ emitted per unit wavelength and per unit mass by a stellar generation of age t' using the most recent version of the Bruzual & Charlot (1993) population synthesis code. This includes all phases of stellar evolution, from the zero-age main sequence to supernova explosions for progenitors more massive than $8 M_\odot$, and to the end of the white dwarf cooling sequence for less massive progenitors. Models can be computed at metallicities $Z = 0.0001, 0.0004, 0.004, 0.008, 0.02, 0.05$, and 0.1 ($Z_\odot = 0.02$). In the models used here, stars evolve along the Padova tracks (Alongi et al. 1993; Bressan et al. 1993; Fagotto et al. 1994a,b,c; Girardi et al. 1996). The tracks include mild overshooting in the convective cores of stars more massive than $1.0 M_\odot$ (with a reduced efficiency between 1.0 and $1.5 M_\odot$), as indicated by various observations of Galactic star clusters. We adopt the semi-empirical library of stellar spectra compiled by Lejeune et al. (1997, 1998) to describe the emission from stars of all metallicities. This library relies on model atmospheres by Kurucz (1992, 1995) for the hotter (O-K) stars with effective temperatures in the range $3,500 < T_{\text{eff}} \leq 50,000$ K, complemented with models by Bessell et al. (1989, 1991) and Fluks et al. (1994) for cooler M giants, and with models by Allard & Hauschildt (1995) for M dwarfs. Lejeune et al. (1997, 1998) used empirical corrections to refine all these models at optical and infrared wavelengths. The spectra of stars hotter than $T_{\text{eff}} = 50,000$ K in the population synthesis models (i.e., a few short-lived Wolf-Rayet stars and central stars of planetary nebulae) are approximated by pseudo-blackbodies, which include the discontinuities across the important photoionization edges blueward of the H-Lyman limit (as parameterized by Shields & Searle 1978 to reproduce the models of Hummer & Mihalas 1970). Nearly all the ionizing radiation from a stellar population with a normal IMF is produced by stars with

$T_{\text{eff}} \gtrsim 30,000$ K. Thus, the results presented in this paper rely heavily on the Kurucz model atmospheres.

The Kurucz (1992, 1995) models are static, plane-parallel atmospheres in local thermodynamic equilibrium (LTE) with line blanketing by over 58 million atomic and molecular transitions. They have been tested against other recent models that include non-LTE effects, spherical geometry, atmospheric expansion, and stellar winds, but which are generally restricted to smaller ranges of temperature and include line blanketing by fewer transitions (Vacca, Garmany & Shull 1996, and references therein; Schaerer & de Koter 1997, and references therein). These comparisons indicate that the Kurucz models produce more H-ionizing photons ($\lambda \leq 912 \text{ \AA}$) than spherical models including non-LTE and wind effects, by an amount that increases from a few percent at $T_{\text{eff}} = 50,000$ K to about 25 per cent at $T_{\text{eff}} = 35,000$ K for main-sequence stars. The Kurucz models produce also less He I-ionizing photons ($\lambda \leq 504 \text{ \AA}$), by an amount that decreases from 40 to 25 per cent in this temperature range. Thus, for a stellar population with a normal IMF, we expect the overall discrepancy in the H- and He I-ionizing continua produced by the two types of models to be less than about 15 and 30 per cent, respectively. This level of accuracy is sufficient for our purposes. In fact, the absolute accuracy of the Kurucz models should be higher, since the effects of line blanketing are probably underestimated in spherical models including non-LTE and wind effects. Unfortunately, observations of the H-ionizing continuum of stars with $T_{\text{eff}} \gtrsim 30,000$ K are not available, while the spectra of two stars with $T_{\text{eff}} \gtrsim 20,000$ K have led to ambiguous interpretations (Cassinelli et al. 1995; Vacca et al. 1996; Schaerer & de Koter 1997). We note that the neglect of wind effects in the Kurucz models may result in a deficiency of He II-ionizing photons ($\lambda \leq 228 \text{ \AA}$; see Schaerer & de Koter 1997). Therefore, we do not rely on the predictions of the population synthesis code at wavelengths blueward of the He II-ionizing edge.

The main adjustable parameters in the population synthesis code are the IMF, the star formation rate, and the metallicity. For simplicity, we assume that the IMF can be approximated by a single power law, $\phi(m) \propto m^{-1-x}$ [defined such that $\phi(m)dm$ is the number of stars born with masses between m and $m+dm$], with an exponent x and lower and upper cutoff masses m_L and m_U . We include m_U as an adjustable parameter and, unless otherwise indicated, adopt a Salpeter IMF ($x = 1.35$) with $m_L = 0.1 M_\odot$. We compute a model spectrum at ages from 1×10^5 yr to 2×10^{10} yr in time steps that increase from 1.5×10^4 yr to 2.5×10^8 yr at late ages. At each time step, the spectrum is defined over the range of wavelengths from 91 \AA to $160 \mu\text{m}$, with samplings of 10 \AA in the ultraviolet, 20 \AA in the visual, and increasing further in the infrared. The lifetimes of the stars producing most of the ionizing radiation are typically $3-5 \times 10^6$ yr at all metallicities. To be conservative, we adopt $t^{\text{OB}} = 1 \times 10^7$ yr in equations (2) and (3), corresponding to a drop by over 99 per cent in the production rate of ionizing photons.

We are also interested in the absorption equivalent widths of the low-order Balmer lines of H I. The spectral resolution of the population synthesis code is too low for line strengths to be measured reliably. We adopt the standard procedure that consists in parameterizing absorption-line strengths as functions of the stellar effective temper-

ature, gravity, and metallicity (e.g., Worthey et al. 1994). This method has been developed mainly to interpret the features of late-type dwarf and giant stars in the spectra of old stellar populations. As a consequence, appropriate calibrations do not exist for the H α and H β absorption equivalent widths of hot-main sequence and supergiant stars that dominate the spectra of young stellar populations. Cananzi, Augarde & Lequeux (1993) did collect accurate H γ and H δ equivalent widths of nearby stars over complete ranges of spectral types and luminosity classes for the specific purpose of population synthesis analyses. Detailed Balmer-line models by Kurucz (1992) indicate that the H α , H β , and H γ equivalent widths of a star are always the same to within 30 per cent and do not depend sensitively on metallicity (see also González-Delgado & Leitherer 1999). We therefore adopt the H γ absorption equivalent widths listed in Table 2 of Cananzi et al. (1993) as estimates of the H α and H β equivalent widths of stars of all metallicities. We compute the line equivalent widths in the integrated spectra of stellar populations by weighting the contributions from individual stars by their level of continuum (see, e.g., Bressan, Chiosi & Tantalo 1996 for a description of this standard procedure).

2.3 Transmission by the Photoionized Gas

We compute the transmission function $T_\lambda^+(t')$ of the gas ionized by stars of age t' (eqs. [1]–[3]) using the standard photoionization code CLOUDY (version C90.04; Ferland 1996). This requires us to specify the parameters of the gas. Here, we adopt ‘effective’ parameters to describe the ensemble of H II regions and the diffuse gas ionized by all stars of age t' within a galaxy. This is motivated by the fact that the optical-line ratios in the integrated spectra of nearby spiral galaxies are similar to those in the spectra of individual H II regions (Kobulnicky et al. 1999; see also §3 below). Thus, photoionization models that reproduce the properties of H II regions should be adequate, modulo some adjustment of the parameters, to reproduce the integrated properties of whole galaxies. For example, at fixed metallicity, the ratio of ionizing-photon to gas densities is expected to be lower when averaged over a whole galaxy than in individual H II regions because of the contribution by diffuse ionized gas (e.g., Lehnert & Heckman 1994; Martin 1997).

In the photoionization code CLOUDY, the gas is described as spherical concentric layers centred on the ionizing source (assumed to be pointlike). The ratio between the radius of the innermost layer r_{in} and the Strömgren radius R_S fixes the actual geometry of a model and the ionization profile of the gas. The Strömgren radius is defined by

$$R_S^3 = 3Q/(4\pi n_H^2 \epsilon \alpha_B), \quad (4)$$

where Q is the rate of ionizing photons, n_H the hydrogen density, ϵ the volume-filling factor of the gas (i.e., the ratio of the volume-averaged hydrogen density to n_H), and α_B the case-B hydrogen recombination coefficient (Osterbrock 1989). The ‘ionization parameter’ is defined as the ratio of ionizing-photon to gas densities at the distance r from the ionizing source,

$$U(r) = Q/(4\pi r^2 n_H c), \quad (5)$$

where c is the speed of light. For $r_{\text{in}} \gtrsim R_S$, the total thickness Δr of the ionized region is much smaller than the Strömgren

radius, $\Delta r \ll R_S$, and the ionization parameter is roughly constant throughout this region, $U(r) \approx U(r_{\text{in}})$. The geometry in this case is approximately plane-parallel, and the volume-averaged ionization parameter is $\langle U \rangle \approx U(r_{\text{in}})$. For $r_{\text{in}} \ll R_S$, however, $U(r)$ is a strong function of r , and the thickness of the ionized region approaches the Strömgren radius, $\Delta r \sim R_S$. The geometry in this case is truly spherical, and the volume-averaged ionization parameter is, assuming constant n_H ,

$$\langle U \rangle \approx 3Q/(4\pi R_S^2 n_H c) = 3U(R_S). \quad (6)$$

Substituting R_S from equation (4) and neglecting the weak dependence of α_B on r through the electron temperature, this yields

$$\langle U \rangle \approx \frac{\alpha_B^{2/3}}{c} \left(\frac{3Q\epsilon^2 n_H}{4\pi} \right)^{1/3}. \quad (7)$$

We find that, at fixed $\langle U \rangle$, our results are not sensitive to the assumed geometry of the gas. For simplicity, we adopt $r_{\text{in}} = 0.01$ pc and hence spherical geometry in all the following applications.

In our approach, the parameters of the photoionization code are effective ones, which describe the ensemble of H II regions and the diffuse gas ionized by a single stellar generation in a galaxy. Since the ionizing radiation changes as the stars evolve, these effective parameters depend on time. We call $\tilde{Q}(t')$ the effective rate of ionizing photons seen by the gas irradiated by stars of age t' throughout the galaxy. For a fixed IMF, $\tilde{Q}(t')$ defines a characteristic mass \tilde{M}_* through the relation

$$\tilde{Q}(t') = \frac{\tilde{M}_*}{hc} \int_0^{\lambda_L} d\lambda \lambda S_\lambda(t'), \quad (8)$$

where $S_\lambda(t')$ is again the luminosity emitted per unit wavelength and per unit mass by a stellar generation of age t' ($\lambda_L = 912$ Å). The quantity \tilde{M}_* should be interpreted as the effective mass of the ionizing star clusters in the galaxy. For simplicity, we assume that the effective density \tilde{n}_H and the effective volume-filling factor $\tilde{\epsilon}$ of the ionized gas do not depend on t' . By analogy with equations (5)–(7), we define the effective ionization parameter of the gas irradiated by stars of age t' and its average over volume as

$$\tilde{U}(t', r) = \tilde{Q}(t')/(4\pi r^2 \tilde{n}_H c), \quad (9)$$

$$\langle \tilde{U} \rangle(t') \approx 3 \tilde{U}(t', R_S) \approx \frac{\alpha_B^{2/3}}{c} \left[\frac{3 \tilde{Q}(t') \tilde{\epsilon}^2 \tilde{n}_H}{4\pi} \right]^{1/3}. \quad (10)$$

Here r and R_S pertain to the H II region ionized by a star cluster of effective mass \tilde{M}_* . In our model, therefore, a galaxy containing several stellar generations comprises different gas components having different effective ionization parameters.

We must also specify the abundances of heavy elements and dust in the gas. The ‘cosmic’ abundances of heavy elements at solar metallicity are constrained to within only a factor of two by observations of Galactic stars (see the discussions by Garnett et al. 1995 and Snow & Witt 1996). As a result, various assumptions can be found in previous photoionization studies about the cosmic abundances of important gas ‘coolants’ such as N, O, and S (e.g., McCall, Rybski & Shields 1985; Campbell 1988; McGaugh 1991; Shields & Kennicutt 1995; Stasińska & Leibler 1995; Leibler & Stasińska 1996).

therer 1996; Tresse et al. 1996; Martin 1997; Bresolin, Kennicutt & Garnett 1999). Here, we adopt the following cosmic abundances for these elements by number relative to hydrogen: $(\text{N}/\text{H})_{\text{cosmic}} = 5.0 \times 10^{-5}$, $(\text{O}/\text{H})_{\text{cosmic}} = 6.6 \times 10^{-4}$, and $(\text{S}/\text{H})_{\text{cosmic}} = 1.3 \times 10^{-5}$. These choices, which are within the ranges considered in the above studies, were motivated in part by the desire to match roughly the observed typical (i.e., median) properties of the samples of nearby galaxies and H II regions investigated in §3. For all the other elements, we adopt the solar-composition abundances of Grevesse & Anders (1989; as extended by Grevesse & Noels 1993). Furthermore, for simplicity, we assume that the abundances of all elements except nitrogen scale linearly with the effective gas metallicity, noted \tilde{Z} . Observations of H II regions in the Milky Way and other nearby galaxies indicate that, at high metallicity, nitrogen is enhanced by secondary nucleosynthetic processing (e.g., Vila-Costas & Edmunds 1993; Henry & Worthey 1999, and references therein). We assume that N/H scales as \tilde{Z}^2 for $\tilde{Z} \geq 0.4Z_{\odot}$, consistent with the observations compiled in Fig. 6 of Henry & Worthey (1999). In all applications in this paper, we adopt the same metallicity for the gas as for the stars (in practice, we adopt the available stellar metallicity closest to that set for the gas).

In our model, we treat the mass fraction of heavy elements locked into dust grains in the ionized gas as a free parameter. We refer to this as the ‘effective dust-to-heavy element ratio’, noted ξ_d . For simplicity, we assume that, at fixed metallicity, the fraction of each refractory element depleted onto dust grains from the gas phase scales linearly with ξ_d (the secondary production of non-refractory nitrogen implies that, when \tilde{Z} changes, this fraction scales almost but not perfectly linearly with ξ_d). For all the elements except silicon, we adopt the default depletion factors of CLOUDY for the average ISM (Cowie & Songaila 1986; Jenkins 1987). These factors correspond to a default dust-to-heavy element ratio of 0.46 for the above cosmic abundances. We adopt the more recent estimate of the silicon depletion factor from *Hubble Space Telescope (HST)* observations of H II regions by Garnett et al. (1995). We take this to correspond to a dust-to-heavy element ratio of 0.30, which is expected to be more typical of H II regions, where grains can be eroded and destroyed (see Garnett et al. 1995; Shields & Kennicutt 1995). The optical properties of the dust in the photoionization code are based on the standard Draine & Lee (1984) grain model with extensions at ionizing wavelengths by Martin & Rouleau (1989). The resulting extinction curve displays a maximum near 17 eV ($\lambda \approx 730 \text{ \AA}$). The most important effect of dust in the photoionized gas is the depletion of coolants (Shields & Kennicutt 1995). Other effects include the absorption and scattering by dust grains of the incident radiation and the photoelectric heating and collisional cooling of the gas (see Ferland 1996 for more details).

Photoionization calculations are often parameterized in terms of the ionization parameter. The reason for this is the similarity of the results obtained for different combinations of Q , ϵ , and n_{H} giving rise to the same $\langle U \rangle$ in equation (7) (e.g., Evans & Dopita 1985; McCall et al. 1985; McGaugh 1991; Stasińska & Leitherer 1996). By analogy, it is convenient here to fix \tilde{M}_* and hence $\tilde{Q}(t')$ (eq. [8]) and use as a variable the value of $\langle \tilde{U} \rangle(t')$ at $t' = 0$ (eq. [10]). We refer to this quantity in the following as the ‘zero-age effective ionization parameter’, noted

$$\langle \tilde{U}_0 \rangle \equiv \langle \tilde{U} \rangle(0). \quad (11)$$

Our results do not depend at all on the choice of \tilde{M}_* (§3.1), except through the fact that any \tilde{M}_* imposes a maximum $\langle \tilde{U}_0 \rangle$ at fixed \tilde{n}_{H} (eqs. [8] and [10]). For all but very high $\langle \tilde{U}_0 \rangle$, therefore, we adopt $\tilde{M}_* = 3 \times 10^4 M_{\odot}$, corresponding to $\tilde{Q}(0) \approx 9 \times 10^{50} \text{ s}^{-1}$ for $m_{\text{U}} = 100 M_{\odot}$ and $\tilde{Z} = Z_{\odot}$ (i.e., the equivalent of roughly 80 O7 V stars; Vacca 1994). This is typical of the rate of ionizing photons in giant H II regions in the Milky Way and other nearby galaxies (e.g., Kennicutt 1984; for $\langle \tilde{U}_0 \rangle \gtrsim 10^{-1.5}$, we adopt $\tilde{M}_* = 1 \times 10^6 M_{\odot}$). For given \tilde{n}_{H} and $\langle \tilde{U} \rangle$, equations (8) and (10) allow us to compute $\tilde{\epsilon}$ (we adopt $\alpha_B = 2.59 \times 10^{-13} \text{ cm}^3 \text{ sec}^{-1}$, appropriate for electronic temperatures $T_e \approx 10^4 \text{ K}$; Osterbrock 1989).

Throughout this paper, we assume that galaxies are ionization bounded. This is suggested by the upper limit of 3 per cent on the fraction of the ionizing radiation escaping from nearby starburst galaxies (Leitherer et al. 1995; see also Giallongo, Fontana & Madau 1997). We stop the photoionization calculations when the electron density falls below 1 per cent of the hydrogen density or if the temperature falls below 100 K. A model H II region, as defined by equation (9), consists typically of an inner zone containing highly-ionized species (e.g., N^{+2} , O^{+2}), an intermediate zone (N^+ , O^+), and an outer zone containing significant H^0 and other neutral and low-ionization species (O^0 , S^+ ; see for example Fig. 1 of Evans & Dopita 1985). The relative sizes of the different zones depend on the model parameters.

2.4 Emergent Luminosity

We have now specified our model for computing the luminosity $L_{\lambda}^+(t)$ produced at the time t by a star-forming galaxy as defined by equation (1). In summary, the main adjustable parameters describing the luminosity S_{λ} emitted by the stars are: the upper cutoff mass of the IMF, m_{U} ; the star formation rate, ψ ; and the metallicity, Z . For the transmission function T_{λ}^+ of the photoionized gas (of effective metallicity $\tilde{Z} = Z$), the main adjustable parameters are: the zero-age effective ionization parameter, $\langle \tilde{U}_0 \rangle$; the effective gas density, \tilde{n}_{H} ; and the effective dust-to-heavy element ratio, ξ_d . The other main parameter is the age of the galaxy, t . In practice, we compute the transmission function T_{λ}^+ of the gas by subdividing star formation into units of mass \tilde{M}_* . This amounts to dividing $\psi(t-t')$ and multiplying $S_{\lambda}(t')$ by \tilde{M}_* in equation (1) and then using equation (8) to evaluate $\tilde{Q}(t')$.

Until now, we have ignored the absorption of photons emanating from the ionized gas (and those emitted by old stars) by dust in the ‘neutral ISM’ before they escape from the galaxy. A detailed modelling of this effect is not necessary if the only observables under interest are the luminosities of optical emission lines, and if at least two H-recombination lines are available. In this case, the observed line luminosities can be corrected in a straightforward way for absorption by dust in the neutral ISM. The reason for this is that the ionized gas always produces H-recombination lines in ratios corresponding to dust-free case B recombination, whether or not dust is present (Hummer & Storey 1992; Ferland 1996; Bottorff et al. 1998; see also §4 below). The effect of dust is to reduce the ionization rate and hence the luminosities of all H-recombination lines by a similar

amount. The departure of H-recombination line ratios (e.g., H α /H β) from dust-free case B recombination is therefore an efficient probe of dust in the neutral ISM of a galaxy. In addition, since most known extinction curves (e.g., Milky Way, LMC, SMC, starburst galaxies) are similar at optical wavelengths, the absorption of other optical emission lines (e.g., [O II], [O III], [N II], [S II]) can be inferred reliably from that of H-recombination lines. In §3.1, we use this remarkable property to calibrate our model for L_λ^+ .

A more refined description of the absorption by dust in the neutral ISM is required to compute simultaneously the line and continuum emission from galaxies. In nearby starburst galaxies, the attenuation inferred from the H α /H β ratio is typically higher than that inferred from the spectral continuum (e.g., Fanelli, O'Connell & Thuan 1988; Calzetti, Kinney & Storchi-Bergmann 1994; Calzetti 1997). Recently, Charlot & Fall (2000) have developed a simple model for the absorption of starlight by dust in galaxies, based on an idealized description of the main features of the ISM. Charlot & Fall show that the finite lifetimes of the dense clouds in which stars form are a key ingredient for resolving the apparent discrepancy between the attenuation of line and continuum photons in nearby starburst galaxies. Their model accounts for all the available observations of these galaxies, including the ratio of far-infrared to ultraviolet luminosities, the H α /H β ratio, the H α equivalent width, and the ultraviolet spectral slope. We use this prescription here to compute the absorption by dust in the neutral ISM.

The luminosity per unit wavelength $L_\lambda(t)$ emerging at time t from a star-forming galaxy can be inferred from the expression of $L_\lambda^+(t)$ in equation (1). We write

$$L_\lambda(t) = \int_0^t dt' \psi(t-t') S_\lambda(t') T_\lambda^+(t') T_\lambda^0(t'), \quad (12)$$

where $T_\lambda^0(t')$ is the transmission function of the neutral ISM. Charlot & Fall (2000) show that the observed relationships between the various integrated spectral properties of nearby starburst galaxies are well reproduced by the simple recipe[†]

$$T_\lambda^0(t') = \exp[-\hat{\tau}_\lambda(t')], \quad (13)$$

$$\hat{\tau}_\lambda(t') = \begin{cases} \hat{\tau}_V (\lambda/5500 \text{ \AA})^{-0.7}, & \text{for } t' \leq 10^7 \text{ yr}, \\ \mu \hat{\tau}_V (\lambda/5500 \text{ \AA})^{-0.7}, & \text{for } t' > 10^7 \text{ yr}. \end{cases} \quad (14)$$

The wavelength dependence of the ‘effective absorption’ curve $\hat{\tau}_\lambda$ is tightly constrained by an observed relation between ratio of far-infrared to ultraviolet luminosities and ultraviolet spectral slope. The age 10^7 yr in the above expression, which coincides with the value of t^{OB} in our model (§2.2), corresponds to the typical timescale for young stars to disrupt their dense ‘birth clouds’ or migrate away from them into the ‘ambient ISM’. Here, we have introduced for convenience the fraction μ of the total effective absorption optical depth in the neutral ISM (birth clouds plus ambient ISM) contributed by the ambient ISM. Charlot & Fall (2000) show that $\mu \approx 1/3$ approximates closely the observed relation between H α /H β ratio and ultraviolet spectral slope

[†] The function denoted here by $T_\lambda^0(t')$ is equivalent to the function $T_\lambda(t')$ defined by equation (6) of Charlot & Fall (2000) for $f = 0.0$ in their notations.

for starburst galaxies. To account for the scatter about this relation, we consider below values ranging from $\mu = 1$ (i.e., all the radiation from the H II regions leaks into the ambient ISM) to $\mu = 1/5$. We note that, for $\hat{\tau}_V = 0$, equations (1) and (12) are equivalent, and $L_\lambda(t) = L_\lambda^+(t)$.

We compute the luminosity $L_\lambda(t)$ as the sum

$$L_\lambda(t) = L_\lambda^c(t) + \sum_i \delta(\lambda - \lambda_i) L_i(t), \quad (15)$$

where $L_\lambda^c(t)$ is the luminosity per unit wavelength of the continuum radiation emerging from the galaxy (including the gas recombination continuum), $L_i(t)$ is the luminosity of the line emerging at the wavelength λ_i , and δ is the Dirac delta function. The equivalent width of an emergent line, noted $W_i(t)$, is the difference between the emission equivalent width [i.e., the ratio of $L_i(t)$ to the continuum luminosity near λ_i] and the stellar absorption equivalent width. In star-forming galaxies, stellar absorption is especially important for H-recombination lines (see §2.2). Finally, we relate the emergent luminosity of an emission line to the star formation rate by the ‘line efficiency factor’

$$\eta_i(t) \equiv L_i(t)/\psi(t). \quad (16)$$

In the following, we are primarily interested in the dependence of $\eta_{\text{H}\alpha}$, $\eta_{[\text{O II}]}$, and $\eta_{[\text{O III}]}$ on the star-formation parameters of galaxies.

3 COMPARISON WITH OBSERVATIONS

In this section, we use observations of nearby star-forming galaxies to calibrate our model. Our goal is to identify models that account for the typical properties, scatter, and trends seen in the observations. In §3.1 below, we first describe the specific influence of each parameter in the model on the ratios of prominent optical emission lines. This allows us to identify how the H α , [O II], and [O III] efficiency factors are related to observed line ratios. This analysis, which involves line luminosities only, does not depend on our assumptions about the absorption by dust in the neutral ISM (§2.4). We must check, however, that the model also reproduces whole (line plus continuum) spectral energy distributions of nearby star-forming galaxies. We show this in §3.2, where we then have to specify the absorption by dust in the neutral ISM.

3.1 Emission-Line Luminosities

To calibrate our model, we compare it with observations of a sample of nearby star-forming galaxies, for which the fluxes of the H α , H β , [O II] $\lambda 3727$, [O III] $\lambda 5007$, [N II] $\lambda 6583$, and [S II] $\lambda\lambda 6717, 6731$ emission lines are available. The sample, which we have compiled from the literature, includes 92 non-Seyfert galaxies spanning a wide range of morphological types, from Sab to Irr, and a wide range of absolute B -band magnitudes, $-16 \lesssim M_B \lesssim -22$ (we adopt a Hubble constant $H_0 = 70 \text{ km s}^{-1} \text{Mpc}^{-1}$). About a third of these (32 galaxies) are normal spiral and irregular galaxies from the sample of Kennicutt (1992b). Another third (33 galaxies) are starburst galaxies selected by Calzetti, Kinney & Storchi-Bergmann (1994) from the *International Ultraviolet Explorer* (IUE) atlas of Kinney et al. (1993), for which optical-line fluxes are

available from Storchi-Bergmann, Kinney & Challis (1995) and McQuade, Calzetti & Kinney (1995). The remaining third (27 galaxies) are low-metallicity, ‘H II galaxies’ (including isolated extragalactic H II regions and blue compact dwarf galaxies) from the sample of Stasińska & Leitherer (1996). These include 17 galaxies with secure H α measurements from the Terlevich et al. (1991) catalogue and 10 galaxies observed by Izotov, Thuan & Lipovetzky (1994). Most of the normal spiral and starburst galaxies in our sample have H α equivalent widths in the range 10–150 Å. The low-metallicity, H II galaxies have typically much higher H α equivalent widths, in the range 300–800 Å.

We correct the flux ratios of all lines for absorption by dust in the neutral ISM on the basis of the observed H α /H β ratios (§2.4). This requires us to first correct the observed H α and H β fluxes for stellar absorption. Calzetti et al. (1994) and Izotov et al. (1994) derive H β stellar absorption equivalent widths for all the galaxies in their samples using the procedure outlined by McCall et al. (1985), that is based on a simultaneous fitting of the observed H α , H β , and H γ fluxes. Also, Kennicutt (1992b) shows that a mean H β absorption equivalent width of –5 Å is appropriate for the galaxies in his sample, and Masegosa et al. (1994) suggest a mean H β absorption equivalent width of –2 Å for the low-metallicity galaxies of the Terlevich et al. (1991) catalogue (this is also roughly the mean value for the galaxies of the Izotov et al. 1994 sample). To correct the observed H α /H β ratio of each galaxy for stellar absorption, we adopt the same absorption equivalent width for H α as for H β (see §2.2 for a justification). We then evaluate the effective absorption by dust in the neutral ISM by comparing the resulting H α /H β ratio to the dust-free case B recombination value of 2.86 (appropriate for electronic densities $n_e \lesssim 10^4$ cm $^{-3}$ and temperatures $T_e \approx 10^4$ K; Osterbrock 1989). Finally, we deredden the relative ratios of the [O II], H β , [O III], H α , [N II], and [S II] lines using the Calzetti (1997) effective absorption curve (which is similar to the Milky Way, LMC, and SMC extinction curves at optical wavelengths). Neglecting possible anisotropies, we equate line flux ratios to the corresponding luminosity ratios. Figs. 1, 2, and 3 show $L_{[\text{O III}]}^+ / L_{\text{H}\beta}^+$ as a function of $L_{[\text{O II}]}^+ / L_{[\text{O III}]}^+$, $L_{[\text{S II}]}^+ / L_{[\text{O III}]}^+$, and $L_{[\text{N II}]}^+ / L_{[\text{S II}]}^+$, respectively, for this sample. Evidently, the galaxies follow well-defined relations in these diagrams. The typical measurement errors indicate that the scatter about the mean relations is real.

We now use these observations to constrain the parameters in our model. Our goal is to identify models that account for the typical properties, scatter, and trends seen in the sample in order to relate the H α , [O II], and [O III] efficiency factors to observed line ratios. The influence of each parameter on observable quantities can best be explored by keeping all other parameters fixed at ‘standard’ values. For simplicity, we take for the moment the star formation rate ψ to be constant. In this case, the age t of the stellar population should be regarded as the effective age of the most recent burst of star formation. After some experimentation, we adopted the following standard parameters:

$$\begin{aligned} t &= 3 \times 10^8 \text{ yr} \\ m_U &= 100 M_\odot \\ \log(\langle \tilde{U}_0 \rangle) &= -2.5 \\ \tilde{Z} &= Z_\odot \end{aligned}$$

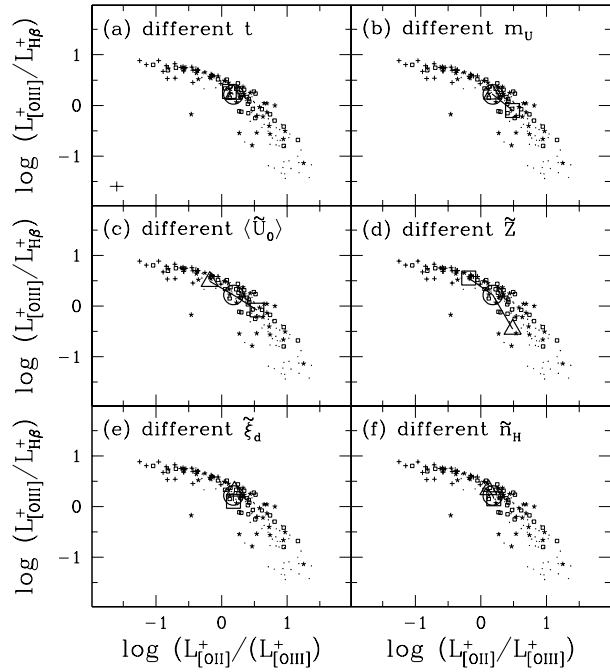


Figure 1. [O III]/H β ratio plotted against [O II]/[O III] ratio. The absorption by dust in the neutral ISM and the stellar H β absorption are not included. The data points are from the samples of galaxies and individual H II regions discussed in §3.1 and are repeated in all panels (squares: normal spiral and irregular galaxies; stars: starburst galaxies; crosses: H II galaxies; and dots: H II regions; typical measurement errors for galaxies are indicated in the upper left panel). In each case, the line shows the effect of varying one parameter from the lower end of the range (square) to the standard value (circle) to the upper end of the range (triangle), with all other parameters fixed at their standard values (eq. [17]): (a) effective starburst age, $t = 1 \times 10^6, 3 \times 10^8$, and 3×10^9 yr; (b) upper cutoff mass of the IMF, $m_U = 40, 100$, and $130 M_\odot$; (c) zero-age effective ionization parameter: $\log(\langle \tilde{U}_0 \rangle) = -3.0, -2.5$, and –2.0; (d) effective metallicity: $\tilde{Z} = 0.2Z_\odot, Z_\odot$, and $2Z_\odot$; (e) effective dust-to-heavy element ratio: $\tilde{\xi}_d = 0.1, 0.3$, and 0.5 (f) effective gas density: $\tilde{n}_H = 3, 30$, and 300 cm^{-3} .

$$\begin{aligned} \tilde{\xi}_d &= 0.3 \\ \tilde{n}_H &= 30 \text{ cm}^{-3}. \end{aligned} \quad (17)$$

While these values are not the result of a rigorous optimization procedure, they do enable the standard model to match roughly the observed typical (i.e., median) properties of the galaxy sample. We note that $\tilde{\xi}_d \approx 0.3$ is of the order of the dust-to-heavy element ratio expected in H II regions (§2.3). Also, $\tilde{n}_H \approx 30 \text{ cm}^{-3}$ is typical of the gas density in Galactic and extragalactic H II regions ($10\text{--}100 \text{ cm}^{-3}$; Osterbrock 1989). For this \tilde{n}_H , $\log(\langle \tilde{U}_0 \rangle) \approx -2.5$ implies $\tilde{\epsilon} \approx 0.04$ (§2.4), which is typical of the volume-filling factor in giant H II regions in the Milky Way and other nearby galaxies (e.g., Kennicutt 1984).

We now compare the predictions of our model with the observations described above. Each panel in Figs. 1–3 shows the effect of increasing and decreasing one parameter with respect to its standard value with the others held fixed. In Fig. 4, we show the influence of these variations on the H α , [O II], and [O III] efficiency factors $\eta_{\text{H}\alpha}$, $\eta_{[\text{O II}]}$, and $\eta_{[\text{O III}]}$ com-

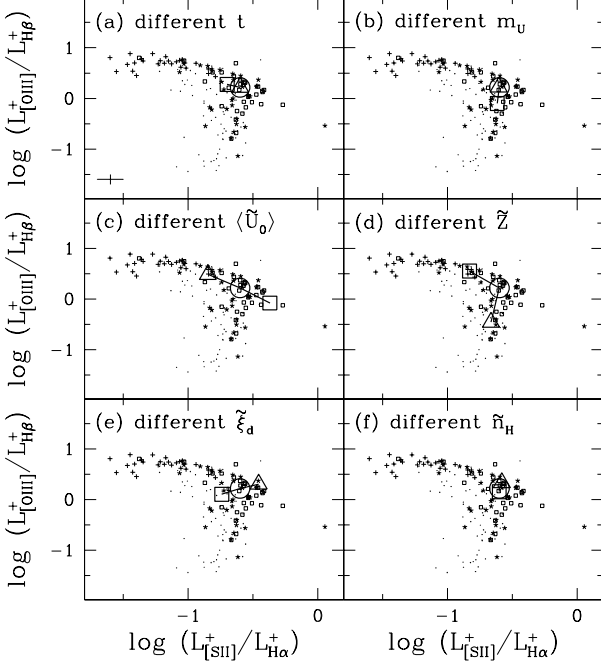


Figure 2. $[\text{O III}]/\text{H}\beta$ ratio plotted against $[\text{S II}]/\text{H}\alpha$ ratio. The absorption by dust in the neutral ISM and the stellar $\text{H}\alpha$ and $\text{H}\beta$ absorptions are not included. The data points are from the samples of galaxies and individual H II regions discussed in §3.1 and are repeated in all panels (squares: normal spiral and irregular galaxies; stars: starburst galaxies; crosses: H II galaxies; and dots: H II regions; typical measurement errors for galaxies are indicated in the upper left panel). In each case, the line shows the effect of varying one parameter from the lower end of the range (square) to the standard value (circle) to the upper end of the range (triangle), with all other parameters fixed at their standard values (eq. [17]). The models are the same as in Fig. 1.

puted using equation (16) with $\hat{\tau}_V = 0$ (i.e., for $L_i = L_i^+$). We can summarize the role of each parameter as follows.

Effective starburst age. Since we have assumed $\psi = \text{const}$, increasing t makes $\eta_{\text{H}\alpha}$, $\eta_{[\text{O II}]}$, and $\eta_{[\text{O III}]}$ larger initially, as massive stars with lifetimes $3-5 \times 10^6$ yr accumulate on the main sequence (Fig. 4a). Stars with ages between 5×10^6 yr and $t^{\text{OB}} = 1 \times 10^7$ yr produce less ionizing photons, while older stars do not contribute to the ionizing radiation in our model (§2). After 1×10^7 yr, therefore, a steady population of H II regions with effective ionization parameters ranging from $\langle \tilde{U}_0 \rangle$ to $\langle \tilde{U} \rangle(t^{\text{OB}})$ is established (eq. [10]). The rising contribution of gas with $\langle \tilde{U} \rangle(t) < \langle \tilde{U}_0 \rangle$ at early ages has a small but significant effect on the line ratios in Figs. 1a–3a, which can be understood from our discussion of $\langle \tilde{U}_0 \rangle$ below.

Upper cutoff mass of the IMF. Increasing m_U makes $\eta_{\text{H}\alpha}$, $\eta_{[\text{O II}]}$, and $\eta_{[\text{O III}]}$ larger because, near the cutoff, more massive stars produce more ionizing photons. This effect becomes negligible for $m_U > 100 M_\odot$ (Fig. 4b). Increasing m_U and hence $\tilde{Q}(t')$ (eq. [8]) also makes the effective ionization parameter larger in the inner (O^{+2}) parts of the H II regions (eq. [9]). At fixed $\langle \tilde{U}_0 \rangle$, however, the effective ionization parameter in the outer, low-ionization (S^+) boundaries near the Strömgren radius is also fixed (eq. [10]). Thus, increasing m_U makes the $[\text{O III}]/\text{H}\beta$ ratio larger and the $[\text{O II}]/[\text{O III}]$

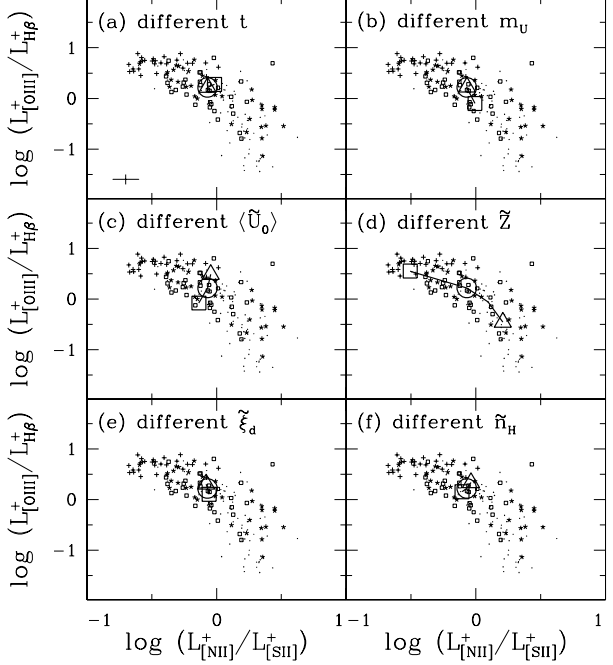


Figure 3. $[\text{O III}]/\text{H}\beta$ ratio plotted against $[\text{N II}]/[\text{S II}]$ ratio. The absorption by dust in the neutral ISM and the stellar $\text{H}\beta$ absorption are not included. The data points are from the samples of galaxies and individual H II regions discussed in §3.1 and are repeated in all panels (squares: normal spiral and irregular galaxies; stars: starburst galaxies; crosses: H II galaxies; and dots: H II regions; typical measurement errors for galaxies are indicated in the upper left panel). In each case, the line shows the effect of varying one parameter from the lower end of the range (square) to the standard value (circle) to the upper end of the range (triangle), with all other parameters fixed at their standard values (eq. [17]). The models are the same as in Fig. 1.

ratio smaller but affects weakly the $[\text{S II}]/\text{H}\alpha$ and $[\text{N II}]/[\text{S II}]$ ratios (Figs. 1b–3b; see §2.3).

Zero-age effective ionization parameter. Increasing $\langle \tilde{U}_0 \rangle$, which corresponds here to increasing $\tilde{\epsilon}$ at fixed \tilde{n}_H and $\tilde{Q}(0)$, causes more gas to be concentrated in the inner, high-ionization parts of the H II regions; thus the $[\text{O III}]/\text{H}\beta$ ratio and $\eta_{[\text{O III}]}$ increase, and the $[\text{O II}]/[\text{O III}]$ ratio and $\eta_{[\text{O II}]}$ decrease (Figs. 1c and 4c). Increasing $\langle \tilde{U}_0 \rangle$ also increases the effective ionization parameter near the Strömgren radius (R_S) and weakens the low-ionization $[\text{S II}]$ line (Figs. 2c and 3c). Since the H-column density scales roughly as $\tilde{\epsilon} \tilde{n}_H R_S \propto \langle \tilde{U} \rangle$, increasing $\langle \tilde{U}_0 \rangle$ at fixed dust-to-gas ratio $\tilde{\xi}_d \tilde{Z}$ causes more ionizing photons to be absorbed by dust and hence reduces $\eta_{\text{H}\alpha}$ (Fig. 4c).

Effective Metallicity. Increasing \tilde{Z} makes the cooling by heavy elements more efficient and reduces the electronic temperature. The cooling becomes dominated by infrared fine-structure transitions with low excitation energies, and fewer electrons are capable of exciting optical lines (e.g., Spitzer 1978). Thus, the $[\text{O III}]/\text{H}\beta$ ratio and $\eta_{[\text{O II}]}$ and $\eta_{[\text{O III}]}$ decline (Figs. 1d and 4d). The $[\text{O II}]/[\text{O III}]$ ratio increases in Fig. 1d because of the efficient fine-structure cooling by doubly-ionized species in the inner parts of the H II regions (Stasińska 1980). The $[\text{S II}]/\text{H}\alpha$ ratio, which increases initially due to the higher S^+ abundance, also declines when

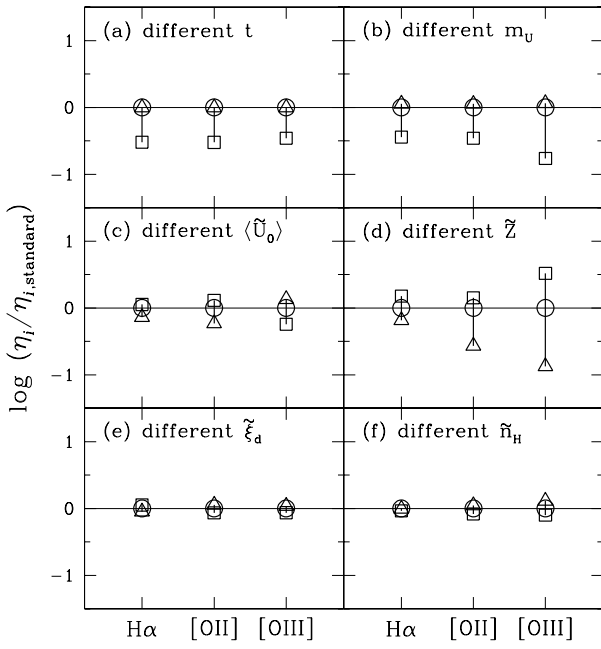


Figure 4. $\text{H}\alpha$, $[\text{O II}]$, and $[\text{O III}]$ efficiency factors (as defined by eq. [16]) normalized to the standard model of eq. [17]. The absorption by dust in the neutral ISM and the stellar $\text{H}\alpha$ absorption are not included. In each panel, the line shows the effect of varying one parameter from the lower end of the range (square) to the standard value (circle) to the upper end of the range (triangle), with all other parameters fixed at their standard values (eq. [17]). The models are the same as in Fig. 1.

cooling becomes important (Fig. 2d). In Fig. 3d, the increase of the $[\text{N II}]/[\text{S II}]$ ratio with \tilde{Z} follows from our inclusion of nitrogen from secondary processing (§2.3). We note that the rate of ionizing photons produced by massive stars tends to decrease with increasing metallicity (e.g., Fig. 4 of García-Vargas et al. 1995). This effect accounts for roughly two thirds of the drop in $\eta_{\text{H}\alpha}$ as \tilde{Z} increases in Fig. 4d, one third arising from the larger fraction of ionizing photons absorbed by dust as $\xi_d \tilde{Z}$ increases.

Effective dust-to-heavy element ratio. Increasing ξ_d depletes important coolants such as oxygen from the gas phase. As the cooling through the infrared fine-structure transitions of these elements declines, the electronic temperature increases and makes cooling through optical transitions more efficient (Shields & Kennicutt 1995). The $[\text{O III}]/\text{H}\beta$ ratio and $\eta_{[\text{O II}]}$ and $\eta_{[\text{O III}]}$ increase only slightly in Figs. 1e and 4e because the rise in T_e is compensated by the depletion of oxygen from the gas phase. However, since S and N are not refractory elements, the $[\text{S II}]/\text{H}\alpha$ ratio increases substantially with ξ_d at roughly constant $[\text{N II}]/[\text{S II}]$ ratio (Figs. 2e and 3e). Increasing ξ_d also causes more ionizing photons to be absorbed by dust and hence reduces $\eta_{\text{H}\alpha}$ (Fig. 4e).

Effective gas density. Increasing \tilde{n}_H makes collisional de-excitation compete with radiative cooling. Since the infrared fine-structure transitions have lower critical densities for collisional de-excitation than the optical transitions, their cooling efficiency declines when increasing \tilde{n}_H (Stasińska 1990). The effect is negligible at low metallicities but more significant at high metallicities, where the fine-structure lines are

the dominant coolants (Oey & Kennicutt 1993). The resulting rise in T_e makes the cooling through optical transitions more important; hence $\eta_{[\text{O II}]}$ and $\eta_{[\text{O III}]}$ increase slightly (Figs. 4f). Changes in \tilde{n}_H have a negligible effect on $\eta_{\text{H}\alpha}$ and a small effect on the line ratios in Figs. 1f–3f.

Other parameters. We have also computed models with different IMF slopes (not shown). Changes in x have a negligible effect on the line ratios, which are determined by the properties of the most massive stars. For a power-law IMF, however, increasing x causes more mass to be locked in low-mass stars and reduces the line efficiency factors. We also tested the influence of changing the effective mass of the ionizing star clusters and found that models with different \tilde{M}_* and fixed $\langle \tilde{U}_0 \rangle$ are virtually identical.

Since each parameter in our model has a specific influence on the ratios of prominent optical emission lines in star-forming galaxies, we can comment on the physical origin of the relations defined by these observed quantities. Figs. 1–3 show that the observed mean trends can be most naturally reproduced by a sequence in the effective gas metallicity, although a spread in the effective ionization parameter is also indicated. In fact, at one end of the observed relations, the very low $[\text{O II}]/[\text{O III}]$ ratios of the H II galaxies with the smallest $[\text{N II}]/[\text{S II}]$ ratios appear to require high effective ionization parameters in addition to low metallicities (Izotov et al. 1994 estimate $\tilde{Z} \approx 0.1 Z_\odot$ from a detailed spectral analysis of these galaxies; this is close to the value $\tilde{Z} = 0.2 Z_\odot$ of the lowest-metallicity model in Figs 1d–3d). At the other end, the $[\text{O III}]/\text{H}\beta$, $[\text{O II}]/[\text{O III}]$, and $[\text{N II}]/[\text{S II}]$ ratios of the most extreme normal spiral and starburst galaxies appear to require low effective ionization parameters in addition to high metallicities. As Figs. 1–3 indicate, the intrinsic scatter about the observed relations can arise from variations in the effective dust-to-heavy element ratio, the effective gas density, and the effective age of the starburst (and possibly the IMF).

The primary dependence of optical emission-line ratios on the metallicity and ionization parameter of the gas is a well-known property of individual H II regions (e.g., Baldwin, Phillips & Terlevich 1981; Evans & Dopita 1985; McCall et al. 1985; Campbell 1988; McGaugh 1991; Shields & Kennicutt 1995; Bresolin et al. 1999). To illustrate the parallel between galaxies and individual H II regions, we also show in Figs. 1–3 observations of 68 H II regions in nearby spiral and irregular galaxies from McCall et al. (1985). The observed relations for H II regions are similar to those for galaxies. This similarity, which justifies a posteriori our adoption of effective parameters to describe the nebular properties of whole galaxies, arises presumably from the limited range of metallicities and ionization parameters of the gas in most star-forming galaxies (e.g., Zaritsky, Kennicutt & Huchra 1994; Kobulnicky et al. 1999). The rough coincidence between starburst and normal spiral galaxies in Figs. 1–3 further suggests that stochastic bursts of star formation do not strongly influence the global gas parameters of galaxies.

Fig. 2 does reveal a difference between the nebular properties of galaxies and those of individual H II regions. At fixed $[\text{O III}]/\text{H}\beta$ ratio, galaxies tend to have higher $[\text{S II}]/\text{H}\alpha$ ratios than individual H II regions. This enhancement in the relative luminosity of the low-ionization $[\text{S II}]$ line is thought to be a signature of the diffuse ionized gas in galaxies (e.g.,

Lehnert & Heckman 1994; Martin 1997; Wang et al. 1997). It is usually associated with enhanced $[\text{O I}]\lambda 6300$, $[\text{N II}]$, and $[\text{O II}]$ emission and reduced $[\text{O III}]$ emission. Fig. 2c confirms that the enhanced $[\text{S II}]/\text{H}\alpha$ ratios of galaxies relative to individual H II regions can be interpreted in terms of a lower effective ionization parameter at fixed effective metallicity. We note, however, that the effective dust-to-heavy element ratio in the ionized gas has also a major influence on the $[\text{S II}]/\text{H}\alpha$ ratio (Fig. 2e). While decreasing $\langle \tilde{U}_0 \rangle$ makes the $[\text{O III}]/\text{H}\beta$ ratio smaller, increasing ξ_d allows models to reproduce the observations of galaxies with both large $[\text{S II}]/\text{H}\alpha$ and $[\text{O III}]/\text{H}\beta$ ratios (the effects of ξ_d on the $[\text{N II}]/\text{H}\alpha$ and $[\text{O I}]/\text{H}\alpha$ ratios are similar to those on the $[\text{S II}]/\text{H}\alpha$ and $[\text{O III}]/\text{H}\beta$ ratios, respectively). It is worth recalling that, in our model, the details of the H II regions and the diffuse gas ionized by each stellar generation in a galaxy are subsumed in our description of the gas by effective parameters.

One of the most important novelties of our model is that it allows us to relate line efficiency factors to observed optical-line ratios. This has fundamental implications for SFR estimates, as can be illustrated by the following example. Figs. 1 and 4 show that increasing $\langle \tilde{U}_0 \rangle$ or decreasing \tilde{Z} relative to our standard model have similar effects on the observed $[\text{O II}]/[\text{O III}]$ and $[\text{O III}]/\text{H}\beta$ ratios, but opposite effects on $\eta_{[\text{O II}]}$. Thus, for fixed $[\text{O II}]/[\text{O III}]$ and $[\text{O III}]/\text{H}\beta$ ratios, there can be a spread of at least a factor of several in $\eta_{[\text{O II}]}$, depending on the effective metallicity and effective ionization parameter of the gas. Fig. 3 shows, however, that the $[\text{N II}]/[\text{S II}]$ ratio can help us distinguish between variations in $\langle \tilde{U}_0 \rangle$ and \tilde{Z} . Therefore, by combining information about the $[\text{O III}]/\text{H}\beta$, $[\text{O II}]/[\text{O III}]$, and $[\text{N II}]/[\text{S II}]$ ratios, we can reduce the uncertainties in $\eta_{[\text{O II}]}$ and hence better constrain the star formation rate. We exploit this property of our model in §4 below, where we construct estimators of the star formation rate for different assumptions about the available spectral information.

3.2 Spectral Energy Distributions

Up to now, we have compared our model with observations only in terms of emission-line luminosities. Since we compute in a consistent way the emission from stars and gas, it is important to check that the model can also reproduce whole (line plus continuum) spectral energy distributions of observed galaxies. This requires us to consider two complications: the contamination of H-recombination lines by stellar absorption; and the absorption of line and continuum photons by dust in the neutral ISM. In §2, we described how these effects are accounted for in our model.

We now compare our model with observed spectral energy distributions of various types of nearby star-forming galaxies. The integrated spectra at wavelengths 3650–7100 Å of the galaxies in the Kennicutt (1992b) sample used in §3.1 are available from Kennicutt (1992a). To avoid using the spectrum of any arbitrary galaxy as reference, we extract observed ‘templates’ from this sample by averaging the spectra of a few galaxies of the same morphological type with roughly similar emission-line properties. Figs. 5, 6, and 7 show such spectral templates for Sb, Sc, and (Magellanic-irregular) Sm/Im galaxies, respectively. Each spectrum is an average over three galaxies with comparable $[\text{O II}]/[\text{O III}]$

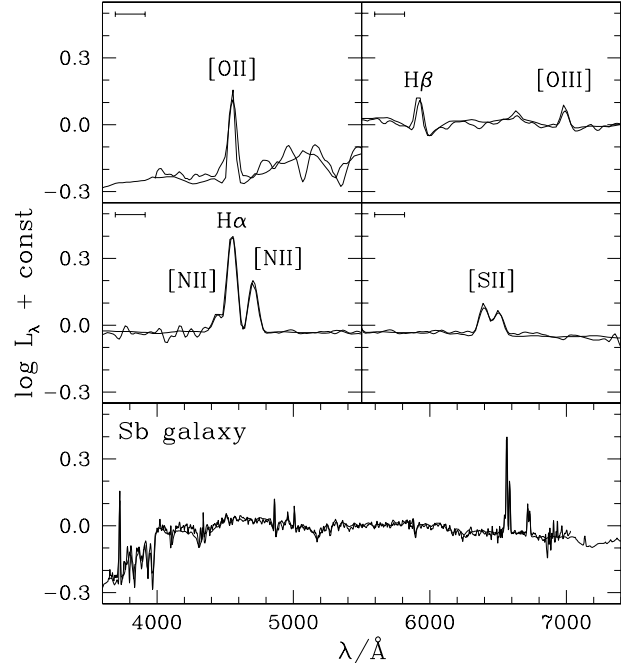


Figure 5. Spectral fit of an observed Sb galaxy template. The template (thin line) is an average over three Sb galaxies with comparable $[\text{O II}]/[\text{O III}]$ and $\text{H}\alpha/\text{H}\beta$ ratios in the Kennicutt (1992a) atlas (NGC 1832, NGC 3147, and NGC 3627). The model (thick line) has an exponentially declining star formation rate (timescale 5 Gyr) and an age $t \approx 9$ Gyr. The gas parameters are: $\log(\langle \tilde{U}_0 \rangle) = -3.0$, $\tilde{Z} = 1.5Z_\odot$, $\xi_d = 0.3$, and $\hat{\tau}_V = 1.0$. The upper four panels show the most prominent lines on a larger wavelength scale (a mark indicates the scale $\Delta\lambda = 30$ Å).

and $\text{H}\alpha/\text{H}\beta$ ratios. For reference, the $[\text{O II}]/[\text{O III}]$ ratios and the $\text{H}\alpha$ and $\text{H}\beta$ equivalent widths of the Sb, Sc, and Sm/Im templates are $L_{[\text{O II}]}/L_{[\text{O III}]} \approx 3.3, 2.6$, and 1.4 , $W_{\text{H}\alpha} \approx 14, 26$, and 82 Å, and $W_{\text{H}\beta} \approx -0.7, 3.0$, and 14 Å, respectively. The spectral resolution is about 800.

To reproduce these observed templates, we use various spectral features to adjust the different parameters in our model. The equivalent widths of emission lines and the stellar continuum (in particular, the 4000 Å discontinuity) constrain the ratio of young (blue) to old (red) stars in the model and hence the star formation history (e.g., Kennicutt 1983; Bruzual & Charlot 1993). In principle, these constraints would depend on the unknown metallicity and the unknown dust content of the galaxies. However, since the star formation history fixes the stellar $\text{H}\alpha$ and $\text{H}\beta$ absorptions, the $\text{H}\alpha/\text{H}\beta$ ratio provides an independent measure of the absorption by dust. Then, using the $[\text{N II}]/[\text{S II}]$ and $[\text{O II}]/[\text{O III}]$ ratios, we can adjust the effective metallicity and the effective ionization parameter of the gas (Figs. 1c and 3d). Finally, for fixed values of these parameters, the $[\text{S II}]/\text{H}\alpha$ ratio constrains the dust content of the ionized gas (Fig. 2e). Therefore, we can tune in a methodic way the parameters of our model to reproduce the observations.

To select models that are consistent with the observations, we explore only a coarse grid of parameters (see Table 1 below). Attempting to fine tune the parameters might be of limited validity because the observed spectral templates were built from individual galaxies that may have

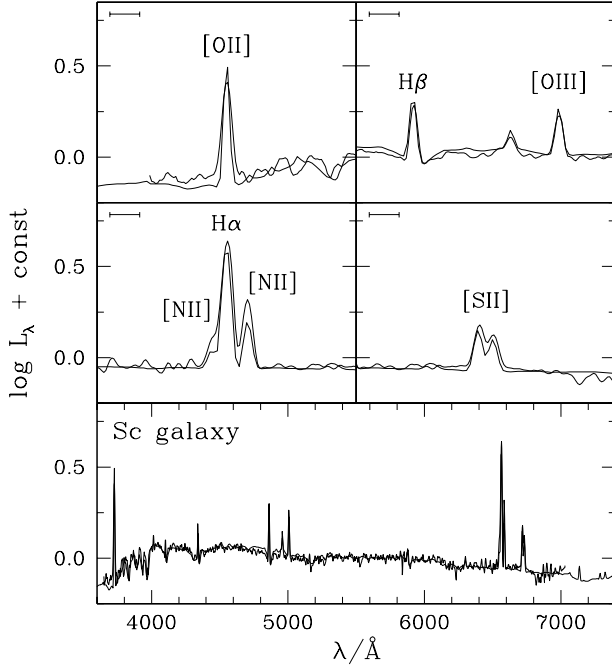


Figure 6. Spectral fit of an observed Sc galaxy template. The template (thin line) is an average over three Sc galaxies with comparable $[\text{O II}]/[\text{O III}]$ and $\text{H}\alpha/\text{H}\beta$ ratios in the Kennicutt (1992a) atlas (NGC 2276, NGC 2903, and NGC 6181). The model (thick line) has an exponentially declining star formation rate (timescale 15 Gyr) and an age $t \approx 8$ Gyr. The gas parameters are: $\log(\langle \tilde{U}_0 \rangle) = -3.0$, $\tilde{Z} = Z_\odot$, $\xi_d = 0.1$, and $\hat{\tau}_V = 0.8$. The upper four panels show the most prominent lines on a larger wavelength scale (a mark indicates the scale $\Delta\lambda = 30$ Å).

slightly different properties. We take the star formation rate $\psi(t)$ to be either constant or exponentially declining. In practice, the results are mostly sensitive to the ratio of the current SFR to the average past SFR. We also explore variations in the zero-age effective ionization parameter, $\langle \tilde{U}_0 \rangle$, the effective metallicity, \tilde{Z} , the effective dust-to-heavy element ratio in the ionized gas, ξ_d , and the effective absorption optical depth at 5500 Å in the neutral ISM, $\hat{\tau}_V$ (eqs. [13] and [14]). We fix the other parameters at their standard values, i.e., $\mu = 1/3$ (eq. [14]), $m_U = 100 M_\odot$, and $\tilde{n}_H = 30 \text{ cm}^{-3}$ (eq. [17]). Figs. 5, 6, and 7 show models selected in this way that reproduce the observed Sb, Sc, and Sm/Im spectral templates. In each case, the continuum spectral energy distribution and the luminosities of all the optical emission lines in the models agree well with the observations. Given the idealizations of the models, we consider these results as very satisfactory. The line strengths in the models are also quantitatively close to those quoted above for the observed spectral templates. For reference, the model Sb, Sc, and Sm/Im spectra, respectively, have $L_{[\text{O II}]}/L_{[\text{O III}]} \approx 2.9$, 2.5, and 1.6, $W_{\text{H}\alpha} \approx 14, 30$, and 89 Å, and $W_{\text{H}\beta} \approx -0.4, 2.3$, and 14 Å. The contribution to these equivalent widths by stellar absorption is $-5.2, -6.2$, and -7.3 Å, respectively.

These spectral fits constrain simultaneously the stars, gas, and dust parameters of the galaxies. We find that the ratio of the current SFR to the average past SFR favored by the observations ranges from 0.4 for the Sb galaxy template to 0.8 for the Sc galaxy template to 1.0 for the Sm/Im galaxy

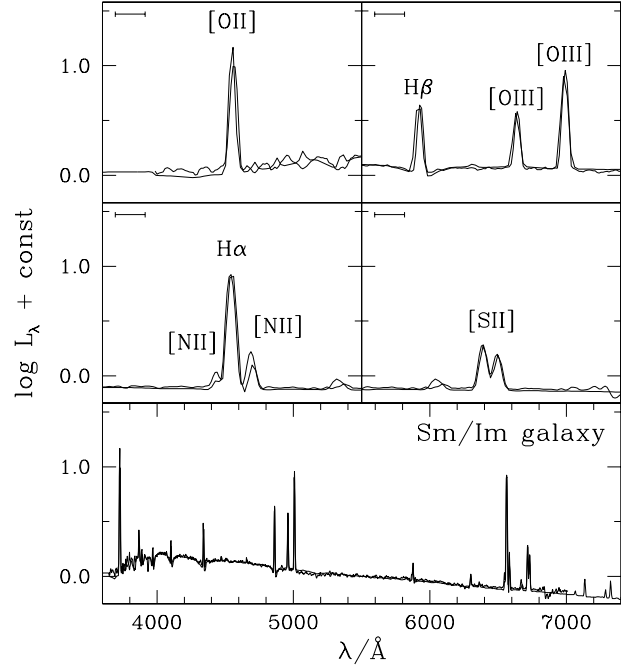


Figure 7. Spectral fit of an observed Sm/Im galaxy template. The template (thin line) is an average over three (Magellanic-irregular) Sm/Im galaxies with comparable $[\text{O II}]/[\text{O III}]$ and $\text{H}\alpha/\text{H}\beta$ ratios in the Kennicutt (1992a) atlas (NGC 4449, NGC 4485, and NGC 4670). The model (thick line) has a constant star formation rate and an age $t \approx 2.5$ Gyr. The gas parameters are: $\log(\langle \tilde{U}_0 \rangle) = -3.0$, $\tilde{Z} = 0.2Z_\odot$, $\xi_d = 0.1$, and $\hat{\tau}_V = 0.1$. The upper four panels show the most prominent lines on a larger wavelength scale (a mark indicates the scale $\Delta\lambda = 30$ Å).

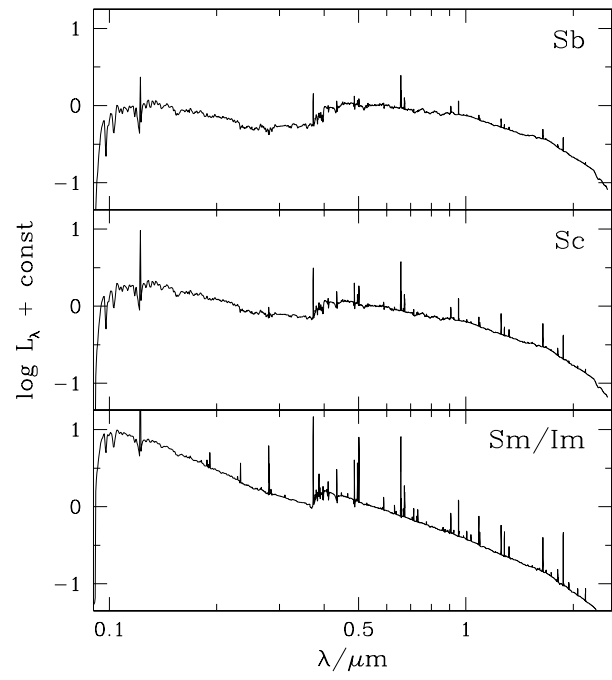


Figure 8. Spectral energy distributions of the same models as in Figs. 5–7 shown with extensions at ultraviolet and near-infrared wavelengths.

template. This is consistent with the expected dependence of this ratio on morphological type (e.g., Kennicutt, Tamblyn & Congdon 1994). Furthermore, the emission-line ratios of the Sb and Sc galaxy templates are well reproduced by models with roughly solar effective metallicity and $\hat{\tau}_V \approx 1$, while the (Magellanic-irregular) Sm/Im galaxy template is better fitted by a model with both low effective metallicity and dust content. All three spectra favor the same zero-age effective ionization parameter, $\langle \tilde{U}_0 \rangle \approx -3.0$, but slightly different effective dust-to-heavy element ratios in the ionized gas. Of course, these are only rough constraints on the star formation properties of the observed galaxies, as we have deliberately avoided fine tuning the model parameters (the uncertainties in the derivation of the physical parameters of galaxies will be addressed in §4). In addition, the observed templates in Fig. 5–7 are representative of only some Sb, Sc, and Sm/Im galaxies (see above). Thus, these results should be taken merely as illustrative of the ability with our model to constrain simultaneously the stars, gas, and dust parameters of galaxies using integrated spectral energy distributions.

We have described here the optical properties of our model for the emission from star-forming galaxies. In reality, we compute spectral energy distributions of the line and continuum emission over the entire range of wavelengths from 91 Å to 5 μm (redward of this limit, the emission from polycyclic aromatic hydrocarbons, which are not included in the model, becomes important). As an example, Fig. 8 shows extensions of the model spectra in Figs. 5–7 at ultraviolet and near-infrared wavelengths. The prominent emission lines outside the optical window (e.g., Mg II at $\lambda = 2798$ Å and [S III], [Fe II], P α at near-infrared wavelengths) offer complementary diagnostics of the star formation parameters, which we plan to study in future work. Finally, it is worth recalling that the prescription we have adopted to describe the absorption by dust in the neutral ISM ensures that our model is also consistent with the observed ultraviolet and far-infrared properties of nearby starburst galaxies (see §2.4 above).

4 OBSERVATIONAL CONSTRAINTS ON THE STARS, GAS, AND DUST PARAMETERS OF GALAXIES

We now have a model for relating the integrated spectral properties of galaxies to physical parameters such as the star formation rate, the metallicity, and the effective absorption optical depth of the dust. In practice, whole spectral energy distributions of the type analyzed in §3.2 are not always available to constrain these parameters in galaxies. However, the tight correlations between the different integrated spectral properties of nearby star-forming galaxies suggest that even partial spectral information may be useful to constrain physical parameters (Figs. 1–3 above; see also Figs. 2 and 3 of Charlot & Fall 2000). Here we analyze these observed relations with our model to construct estimators of the star formation rate, the gas-phase oxygen abundance, and the effective absorption optical depth of the dust in galaxies for various assumptions about the available spectral information.

Our first step is to select a comprehensive set of models that account for the full range of observations of nearby

star-forming galaxies. We use the observed emission-line ratios of the galaxies in Figs. 1–3 to identify the appropriate ranges in zero-age effective ionization parameter, $\langle \tilde{U}_0 \rangle$, effective metallicity, \tilde{Z} , and effective dust-to-heavy element ratio, $\tilde{\xi}_d$. Since the effective gas density has only a weak influence on line luminosities (Figs. 1f–4f), we fix this parameter at its standard value of equation (17), i.e., $\tilde{n}_H = 30 \text{ cm}^{-3}$. We also consider variations in the total effective absorption optical depth of the dust in the neutral ISM, $\hat{\tau}_V$, and the fraction of this contributed by the ambient ISM, μ (eq. [14]). These are constrained by the observed relations between ratio of far-infrared to ultraviolet luminosities, H α /H β ratio, and ultraviolet spectral slope in nearby starburst galaxies (Charlot & Fall 2000). Finally, we consider different star formation histories (as before, we assume that stars and gas have the same metallicity, i.e., $Z = \tilde{Z}$). We take the star formation rate $\psi(t)$ to be either constant or exponentially declining. In each case, we compute models at ages ranging from 10^7 yr to 10^{10} yr. For simplicity, we adopt in all models a Salpeter IMF truncated at 0.1 and $100 M_\odot$ (the line efficiency factors in Table 2 below would be a factor of about 3.4 times smaller for a Scalo 1986 IMF with the same cutoff masses).

In Table 1, we report the parameters of the models found to reproduce the observations of nearby star-forming galaxies. Most but not all combinations of these parameters are consistent with the observations. In particular, the observed emission-line ratios of nearby galaxies (Figs. 1–3) do not favor combinations of both either very low or very high \tilde{Z} and $\langle \tilde{U}_0 \rangle$. In Fig. 9, we show the emission-line ratios of the models with the allowed combinations of \tilde{Z} , $\langle \tilde{U}_0 \rangle$, and $\tilde{\xi}_d$ in Table 1. As in Figs. 1–3, we do not include in Fig. 9 the absorption by dust in the neutral ISM and the stellar H α and H β absorptions. Since age has a negligible effect in such diagrams (especially for $t \geq 10^7$ yr; see Figs. 1a–3a), we plot only models with constant $\psi(t)$ at the standard age $t = 3 \times 10^8$ yr (eq. [17]). Fig. 9 shows that the models in Table 1 account well for the typical properties, scatter, and trends seen in the observations. The models do not reach the extreme [N II]/[S II] ratios of some H II and starburst galaxies, suggesting that our simple prescription for secondary nitrogen production may break down at very low and very high \tilde{Z} (§2.3; we note that the largest observed [N II]/[S II] ratios in Fig. 9c could result from a decrease in the S/O abundance ratio at high metallicity; see Díaz et al. 1991). We have checked that the predictions of our model at these extreme effective metallicities do not affect our conclusions below. The models with various $\hat{\tau}_V$ and μ in Table 1 are also consistent, by construction, with the observed ratios of far-infrared to ultraviolet luminosities, H α /H β ratios, and ultraviolet spectral slopes of nearby starburst galaxies in Figs. 2–4 of Charlot & Fall (2000; see §2.4 above). Therefore, the models in Table 1 enable us to interpret the observed spectral properties of nearby star-forming galaxies in terms of stars, gas, and dust parameters.

A striking property of these models is that they span vast ranges of H α and [O II] efficiency factors, $\eta_{H\alpha} = 0.05\text{--}2.8 \times 10^{15} \text{ erg g}^{-1}$ and $\eta_{[O\text{ II}]} = 0.02\text{--}3.6 \times 10^{15} \text{ erg g}^{-1}$ (for $W_{H\alpha}$ and $W_{[O\text{ II}]}$ both larger than 5 Å). Only parts of these ranges arise from variations in $\hat{\tau}_V$ and μ in Table 1. For $\hat{\tau}_V = 0$, changes in the ionized-gas parameters alone (\tilde{Z} , $\langle \tilde{U}_0 \rangle$, and $\tilde{\xi}_d$) account for factors of 3.5 and 14 spreads in $\eta_{H\alpha}$ and $\eta_{[O\text{ II}]}$, respectively. The range of stel-

Table 1. Parameters of the models reproducing the observed integrated spectral properties of nearby star-forming galaxies.

$\log(\langle \tilde{U}_0 \rangle)$	-3.0, -2.5, -2.0, -1.5
\tilde{Z}/Z_\odot	0.2, 0.5, 0.75, 1.0, 1.5, 2.0
ξ_d	0.1, 0.3, 0.5
$\hat{\tau}_V$	0.01, 0.3, 0.5, 1.0, 1.5, 2.0
μ^{-1}	1, 3, 5
$\psi(t)$	constant, exponentially declining
t/yr	10^7 – 10^{10} (112 uneven steps)

Two timescales are adopted for the exponentially declining star formation rate $\psi(t)$: 0.1 and 6.0 Gyr. All models have $\tilde{n}_H = 30 \text{ cm}^{-3}$ and a Salpeter IMF truncated at 0.1 and $100 M_\odot$. Most but not all combinations of the above parameters are allowed by the observations (see text for detail).

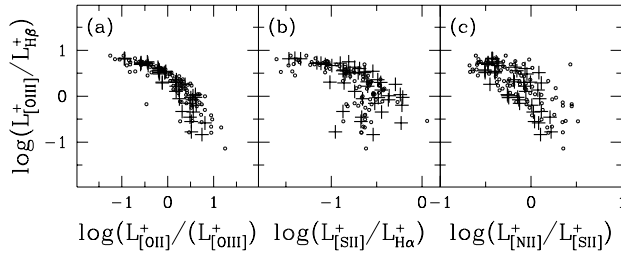


Figure 9. Emission-line ratios of the models in Table 1. The absorption by dust in the neutral ISM and the stellar H α and H β absorptions are not included. Only models with constant $\psi(t)$ are shown at the standard age $t = 3 \times 10^8 \text{ yr}$ (eq. [17]; crosses). The data points in (a), (b), and (c) are the same galaxies as in Figs. 1, 2, and 3, respectively (all types plotted as circles here).

lar H α absorption strengths arising from variations in the star formation history contributes an additional factor of 1.8 spread in $\eta_{H\alpha}$. These results put into perspective the approximate efficiency factors often adopted to estimate star formation rates in galaxies, e.g., $\eta_{H\alpha} \approx 2.0 \times 10^{15} \text{ erg g}^{-1}$ and $\eta_{[O\text{II}]} \approx 1.2 \times 10^{15} \text{ erg g}^{-1}$ (Kennicutt 1998). Our model allows us to assess that the actual uncertainties in SFR estimates based on either the H α line or the [O II] line alone can be as high as several decades.

Since we know how $\eta_{H\alpha}$ and $\eta_{[O\text{II}]}^0$ are related to observed optical-line ratios (§3.1), we can exploit this information to improve SFR estimates in galaxies. For the sake of generality, we denote here by \mathcal{A} the quantity to be estimated (e.g., $\eta_{H\alpha}$, $\eta_{[O\text{II}]}^0$). Given a set of N spectral features x_k (e.g., line ratios, equivalent widths), we can always least-squares fit to the models in Table 1 an expression of \mathcal{A} of the form

$$\log \mathcal{A} \approx a_0 + \sum_{k=1}^N a_k \log x_k, \quad (18)$$

where the a_k are the fitting coefficients. It is convenient to introduce the logarithmic difference Δ_m between the true and fitted \mathcal{A} values of the m th model,

$$\Delta_m = \log \mathcal{A}_m - a_0 - \sum_{k=1}^N a_k \log x_{k,m}. \quad (19)$$

The probability distribution of the models being unknown, the maximum absolute value of Δ_m over all the models in Table 1 provides a lower limit on the accuracy of expression (18). By experimenting with several different combina-

tions of spectral features x_k , we can identify the one leading to the highest accuracy and hence the best observational estimate of \mathcal{A} .

We have used this procedure to derive estimators of not only the H α and [O II] efficiency factors, but also the gas-phase oxygen abundance and the effective absorption optical depth of the dust in star-forming galaxies. In Table 2, we present our results for several examples of available spectral information (cases A–G). The observations are assumed *not* to be corrected for dust and stellar (H-Balmer) absorption. In each case, we express the efficiency factor of the most accurate SFR tracer ($\eta_{H\alpha}$, $\eta_{H\alpha+[N\text{II}]}$, or $\eta_{[O\text{II}]}$), the gas-phase oxygen abundance (O/H), and the effective dust-absorption factor at 5500 Å ($e^{-\hat{\tau}_V}$) as functions of the available spectral features. For reference, we also give the expression of the line efficiency factor for $\hat{\tau}_V = 0$ (noted $\eta_{H\alpha}^0$, $\eta_{H\alpha+[N\text{II}]}^0$, or $\eta_{[O\text{II}]}^0$).

The accuracy of an estimator in Table 2 depends on its regime of application. In Fig. 10, we plot for each estimator the range in Δ_m , as defined by equation (19), as a function of the estimated quantity. The potential (logarithmic) error in an estimate of η_i , O/H, or $e^{-\hat{\tau}_V}$ – ignoring observational errors – is the maximum absolute value of Δ_m at the abscissa corresponding to that estimate (we note that, for $e^{-\hat{\tau}_V} \sim 1$, even small values of $|\Delta_m|$ can translate into large errors in $\hat{\tau}_V$). The maximum absolute value of Δ_m over the full range in the estimated quantity is the maximum error associated to the estimator. To avoid the undue influence of large tails arising from a few discrepant models in the $|\Delta_m|$ distributions, we define the ‘uncertainty’ pertaining to each estimator in Fig. 10 as the 99th percentile range in $|\Delta_m|$ over the full range in the estimated quantity. We report this uncertainty in Table 2 and use it below to quantify the accuracy of an estimator (for reference, we also indicate in parentheses in Table 2 the full, 100th percentile range in $|\Delta_m|$).

The results of Table 2 demonstrate the merit of spectral information for estimating the star formation rate, the metallicity, and the absorption by dust in a galaxy. In the best-constrained case where the [O II], H β , [O III], H α , [N II], and [S II] lines are all observed (case A), we find that $\eta_{H\alpha}$, O/H, and $e^{-\hat{\tau}_V}$ can be estimated to within less than a factor of 2 (i.e., with absolute logarithmic uncertainties less than 0.3). This is a reduction by more than a factor of 25 of the uncertainty in $\eta_{H\alpha}$ relative to the case where the H α line alone is used to estimate the SFR (see above). The reason for such an improvement is that we have included in the estimator the H α /H β , [O II]/[O III], [O III]/H β , and [S II]/H α ratios and the H β equivalent width, which all carry important information about the parameters that influence $\eta_{H\alpha}$ (see §3). Remarkably, a similar accuracy in $\eta_{H\alpha}$ can be achieved even if the H α line is blended with the adjacent [N II] lines (case B). In this case, however, the loss of the [N II]/[S II] ratio makes O/H estimates based on the [O III]/H β and [O II]/[O III] ratios more uncertain, especially for low O/H (see Fig. 10; we do not discuss here the [O III] $\lambda 4363$ line, which is a diagnostic of low oxygen abundance but is very weak in most galaxies; see Kobulnicky et al. 1999 and Figs. 5–7 above). In case C, the unavailability of H β (and hence H α /H β) makes the uncertainties in $e^{-\hat{\tau}_V}$ larger, but $\eta_{H\alpha}$ and O/H can still be determined to within a factor of 2–3 using the [O II], [O III], H α , and [N II] lines. As above, we find that the blending of H α with the adjacent

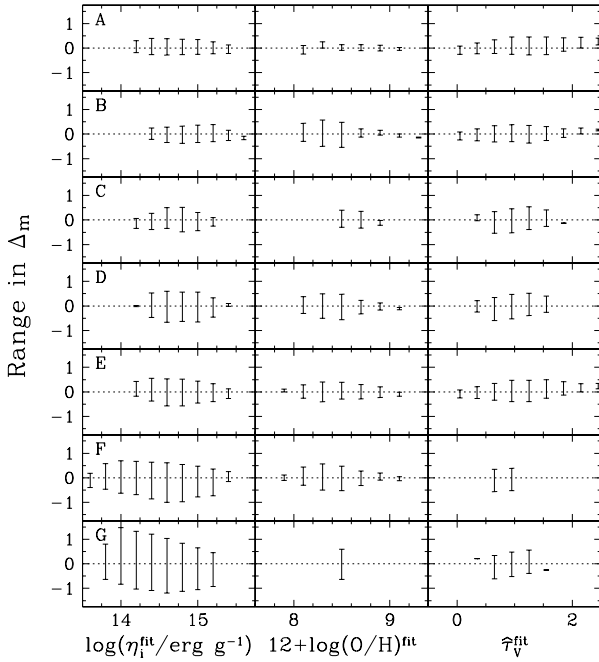


Figure 10. Range in the logarithmic error Δ_m (as defined by eq. [19]) obtained when applying the formulae in Table 2 to the models in Table 1, plotted against estimated line efficiency factor, gas-phase oxygen abundance, and effective absorption optical depth of the dust. Each panel row corresponds to a different case in Table 2, as indicated.

[N II] lines affects only weakly the accuracy in $\eta_{H\alpha}$ (case D). In the case where the $H\beta$ line is observed but the [O II] line is not (case E), $\eta_{H\alpha}$ and O/H can again be estimated to within a factor of 2–3 using the $H\beta$, [O III], $H\alpha$, and [N II] lines, while the $H\alpha/H\beta$ ratio helps constrain $e^{-\hat{\tau}_v}$.

A critical situation arises when the $H\alpha$ line is not available (cases F and G in Table 2). We find that, in this case, the star formation rate cannot be determined reliably from the [O II], $H\beta$, and [O III] lines and the 4000 Å discontinuity. Using all these features, we did not succeed in estimating $\eta_{[O\,II]}$ (or $\eta_{H\beta}$ or $\eta_{[O\,III]}$) to within less than a factor of 5 (case F). In the case where only [O II] and D_{4000} are available (case G), the uncertainty in $\eta_{[O\,II]}$ reaches a factor of almost 10, and O/H is unconstrained (Fig. 10). The major source of uncertainties in $\eta_{[O\,II]}$ estimates is the lack of a strong dust discriminant in the wavelength interval between [O II] and [O III]. The uncertainties in $\eta_{[O\,II]}^0$ in cases F and G demonstrate that, without dust, the [O II] efficiency factor can be constrained to within a factor of only 2–3 based simply on the [O II] equivalent width and the 4000 Å discontinuity. As a further check, we reestimated $\eta_{[O\,II]}$ in case F after reducing the ranges in zero-age effective ionization parameter and effective metallicity of the models in Table 2 to $0.5 Z_\odot \leq \tilde{Z} \leq Z_\odot$ and $-3.0 \leq \log(\langle \tilde{U}_0 \rangle) \leq -2.0$. The resulting uncertainty was 0.65, comparable to the value of 0.70 in Table 2. We note in Fig. 10 that $\eta_{[O\,II]}$ estimates are slightly more accurate for $\eta_{[O\,II]} \lesssim 10^{14} \text{ erg g}^{-1}$, corresponding to galaxies with high effective metallicity and high dust content, and $\eta_{[O\,II]} \gtrsim 10^{15} \text{ erg g}^{-1}$, corresponding to galaxies with low effective metallicity and low dust content.

Independent constraints on the absorption by dust in

a galaxy are not expected to improve significantly SFR estimates based on the [O II] luminosity. In nearby starburst galaxies, the correlation between ratio of far-infrared to ultraviolet luminosities and ultraviolet spectral slope sets tight constraints on the effective absorption optical depth of the dust at ultraviolet wavelengths (e.g., Meurer, Heckman & Calzetti 1999; Charlot & Fall 2000). However, the different attenuation of line and continuum photons in these galaxies (accounted for by values of μ^{-1} greater than unity in Table 1; see §2.4) make corrections of the [O II] luminosity uncertain. This is all the more critical in that the [O II] equivalent width is needed to estimate $\eta_{[O\,II]}^0$ (Table 2). We therefore conclude that, without the $H\alpha$ line, the SFR is difficult to estimate from the optical emission of a galaxy.

It is worth recalling that the estimators in Table 2 neglect the potential contribution by active galactic nuclei to the ionizing radiation in galaxies. The presence of an AGN in a galaxy is usually revealed by readily identifiable signatures. These include larger [O III]/ $H\beta$ and [S II]/ $H\alpha$ ratios than in the galaxies in Fig. 2 and strong emission lines of highly-ionized species, such as [Ne V] $\lambda 3426$ and [Fe VII] $\lambda 6087$, which are generally not produced by the softer spectra of stellar populations (e.g., Osterbrock 1989). Furthermore, the broad emission lines of most AGNs have velocity widths (FWHMs of several thousand km s^{-1}) that are several times larger than those expected from the virial motions within galaxies (FWHMs less than about 1000 km s^{-1} , corresponding to line-of-sight velocity dispersions less than about 400 km s^{-1}). Hence, the contamination of the nebular emission from a galaxy by an AGN can usually be identified.

5 CONCLUSIONS

We have developed a model for computing consistently the line and continuum emission from galaxies, based on an idealized description of the H II regions and the diffuse gas ionized by single stellar generations in a galaxy. We have calibrated the nebular properties of this model using the observed [O III]/ $H\beta$, [O II]/[O III], [S II]/ $H\alpha$, and [N II]/[S II] ratios of a representative sample of nearby spiral and irregular, starburst, and H II galaxies. To compute whole (line plus continuum) spectral energy distributions, we have included the absorption by dust in the neutral ISM using a recent simple prescription, which is consistent with observations of nearby starburst galaxies. The model succeeds in reproducing quantitatively the optical spectra of nearby galaxies of various types. The prime parameters in our model, including the star formation history, the zero-age effective ionization parameter, the effective gas metallicity, the effective dust-to-heavy element ratio in the ionized gas, and the effective optical depth of the dust in the neutral ISM (and the fraction of this contributed by the ambient ISM) each have a specific influence on the integrated line and continuum properties of galaxies. Optical spectral fits enable us, in turn, to constrain simultaneously the star formation history, the metallicity, and the absorption by dust in galaxies.

We have used this model to derive new estimators of the $H\alpha$ and [O II] efficiency factors ($\eta_{H\alpha}$ and $\eta_{[O\,II]}$), the gas-phase oxygen abundance, and the effective absorption optical depth of the dust in star-forming galaxies. The observed integrated spectral properties of nearby galaxies are com-

Table 2. Estimators of the H α and [O II] efficiency factors, the gas-phase oxygen abundance, and the effective absorption optical depth of the dust in galaxies for different assumptions about the available spectral information (cases A–G).

Case	Available spectral information ^a						Diagnostics ^b and estimators ^c	Uncertainty ^d (logarithmic)	
	[O II]	D ₄₀₀₀	H β	[O III]	H α	[N II]	[S II]		
A	yes	yes	yes	yes	yes	yes	$\eta_{H\alpha} = 1.85 \times 10^{15} x_1^{-2.25} x_2^{1.46} x_3^{0.90} x_4^{-1.14} x_5^{-0.15}$ O/H = $5.09 \times 10^{-4} x_2^{0.17} x_6^{1.17}$ $e^{-\hat{\tau}_V} = 1.20 x_1^{-3.32} x_2^{1.06} x_3^{0.62} x_4^{-0.85} x_5^{-0.49}$ $\eta_{H\alpha}^0 = 1.44 \times 10^{15} x_1^{0.75} x_3^{-0.17} x_5^{0.15} x_6^{-0.58}$	0.26 (0.39) 0.24 (0.26) 0.27 (0.46) 0.14 (0.20)	
B	yes	yes	yes	yes	blended ^e	yes	$\eta_{H\alpha+[N II]} = 2.29 \times 10^{15} x_2^{1.80} x_3^{1.04} x_7^{-1.40} x_8^{-1.35}$ O/H = $4.21 \times 10^{-4} x_2^{0.51} x_3^{-0.24} x_8^{-0.42}$ ($L_{[O II]}/L_{[O III]} < 0.8$) O/H = $4.58 \times 10^{-4} x_3^{-0.37} x_8^{-0.54}$ ($L_{[O II]}/L_{[O III]} \geq 0.8$) $e^{-\hat{\tau}_V} = 0.90 x_2^{2.01} x_3^{1.21} x_7^{-1.41} x_8^{-1.70}$ $\eta_{H\alpha+[N II]}^0 = 2.31 \times 10^{15} x_2^{0.28} x_3^{0.12} x_7^{-0.36} x_8^{-0.06}$	0.33 (0.39) 0.52 (0.58) 0.21 (0.26) 0.32 (0.38) 0.25 (0.26)	
C	yes	yes	no	yes	yes	yes	...	$\eta_{H\alpha} = 1.36 \times 10^{15} x_2^{0.38} x_9^{0.80} x_{10}^{-0.40} x_{11}^{0.33}$ O/H = $3.98 \times 10^{-4} x_2^{-0.21} x_{10}^{0.39}$ $e^{-\hat{\tau}_V} = 0.64 x_2^{-0.12} x_9^{0.62} x_{11}^{0.20}$ $\eta_{H\alpha}^0 = 1.69 \times 10^{15} x_2^{0.64} x_9^{-0.10} x_{10}^{-0.45} x_{11}^{0.09}$	0.41 (0.52) 0.31 (0.40) 0.49 (0.54) 0.12 (0.15)
D	yes	yes	no	yes	blended ^e	...	$\eta_{H\alpha+[N II]} = 2.99 \times 10^{15} x_2^{-0.12} x_{12}^{0.86} x_{13}^{0.68}$ O/H = $4.32 \times 10^{-4} x_2^{0.13} x_{14}^{-0.43}$ ($L_{[O II]}/L_{[O III]} < 0.8$) O/H = $3.63 \times 10^{-4} x_2^{-0.57} x_{14}^{-0.72}$ ($L_{[O II]}/L_{[O III]} \geq 0.8$) $e^{-\hat{\tau}_V} = 0.82 x_2^{-0.17} x_{12}^{0.61} x_{13}^{0.35}$ $\eta_{H\alpha+[N II]}^0 = 2.09 \times 10^{15} x_{13}^{0.14} x_{14}^{-0.13}$	0.52 (0.66) 0.52 (0.56) 0.27 (0.41) 0.50 (0.59) 0.25 (0.30)	
E	yes	yes	yes	yes	...	$\eta_{H\alpha} = 1.71 \times 10^{15} x_1^{-2.96} x_3^{-0.12} x_5^{-0.17} x_{10}^{-0.18} x_{11}^{-0.38}$ O/H = $4.15 \times 10^{-4} x_3^{-0.29} x_{10}^{0.40}$ ($L_{[O III]}/L_{H\beta} \leq 2.5$) O/H = $4.15 \times 10^{-4} x_3^{-0.29} x_{10}^{0.40}$ ($L_{[O III]}/L_{H\beta} > 2.5$) $e^{-\hat{\tau}_V} = 1.15 x_1^{-3.97} x_3^{-0.01} x_5^{-1.21} x_{10}^{0.01} x_{11}^{0.52}$ $\eta_{H\alpha}^0 = 1.34 \times 10^{15} x_1^{2.18} x_3^{-0.12} x_5^{2.44} x_{10}^{-0.17} x_{11}^{-2.13}$	0.45 (0.57) 0.32 (0.33) 0.40 (0.40) 0.35 (0.49) 0.21 (0.35)
F	yes	yes	yes	yes	$\eta_{[O II]} = 6.92 \times 10^{14} x_2^{-0.02} x_5^{0.41} x_{15}^{1.52}$ O/H = $3.78 \times 10^{-4} x_2^{0.17} x_3^{-0.44}$ ($L_{[O II]}/L_{[O III]} < 0.8$) O/H = $3.96 \times 10^{-4} x_3^{-0.46}$ ($L_{[O II]}/L_{[O III]} \geq 0.8$) $e^{-\hat{\tau}_V} = 0.47 x_2^{0.05} x_5^{0.01}$ $\eta_{[O II]}^0 = 1.43 \times 10^{15} x_2^{-1.01} x_3^{-1.03} x_5^{-1.21} x_{16}^{1.99}$	0.70 (0.99) 0.51 (0.57) 0.31 (0.31) 0.55 (0.56) 0.20 (0.40)
G	yes	yes	$\eta_{[O II]} = 4.44 \times 10^{14} x_{16}^{0.73} x_{17}^{1.87}$ O/H = $3.34 \times 10^{-4} x_{17}^{-0.23}$ $e^{-\hat{\tau}_V} = 0.47 x_{16}^{0.10} x_{17}^{-0.86}$ $\eta_{[O II]}^0 = 1.21 \times 10^{15} x_{16}^{0.89} x_{17}^{3.78}$	0.94 (1.47) 0.63 (0.63) 0.56 (0.61) 0.39 (0.96)

^a Observed line luminosities and D₄₀₀₀ (as defined by Bruzual 1983) not corrected for dust and stellar (H-Balmer) absorption. A ‘yes’ means that the observed rest-frame equivalent width of the line exceeds 5 Å, a ‘no’ that the equivalent width is less than this limit, and an ellipsis that the line is not observed. The lines are [O II] λ 3727, [O III] λ 5007, [N II] λ 6583 (see however footnote *e*), and [S II] $\lambda\lambda$ 6717, 6731.

^b The basis functions x_k are spectral features normalized to the same standard model as in eq. [17] but including the effects of stellar H α and H β absorption (for $\hat{\tau}_V = 0$): $x_1 \equiv (L_{H\alpha}/L_{H\beta})/3.4$; $x_2 \equiv (L_{[O II]}/L_{[O III]})/1.5$; $x_3 \equiv (L_{[O III]}/L_{H\beta})/2.0$; $x_4 \equiv (L_{[S II]}/L_{H\alpha})/0.26$; $x_5 \equiv W_{H\beta}/(25 \text{ \AA})$; $x_6 \equiv (L_{[N II]}/L_{[S II]})/0.85$; $x_7 \equiv (L_{H\alpha+[N II]}/L_{H\beta})/4.5$; $x_8 \equiv (L_{[S II]}/L_{H\alpha+[N II]})/0.20$; $x_9 \equiv (L_{[O II]}/L_{H\alpha})/0.90$; $x_{10} \equiv (L_{[N II]}/L_{H\alpha})/0.22$; $x_{11} \equiv W_{H\alpha}/(170 \text{ \AA})$; $x_{12} \equiv (L_{[O II]}/L_{H\alpha+[N II]})/0.70$; $x_{13} \equiv W_{H\alpha+[N II]}/(220 \text{ \AA})$; $x_{14} \equiv (L_{[O III]}/L_{H\alpha+[N II]})/0.45$; $x_{15} \equiv (L_{[O II]}/L_{H\beta})/3.0$; $x_{16} \equiv W_{[O II]}/(60 \text{ \AA})$; $x_{17} \equiv D_{4000}/1.1$.

^c Line efficiency factors $\eta_{H\alpha}$, $\eta_{[O II]}$, and $\eta_{H\alpha+[N II]}$ in units of erg g⁻¹ (eq. [16]); oxygen abundance by number relative to hydrogen in the ionized gas after accounting for the depletion onto dust grains ([O/H]_{cosmic} = 6.6×10^{-4}]; and effective dust-absorption factor $e^{-\hat{\tau}_V}$ at 5500 Å (eqs. [13] and [14]). The line efficiency factors $\eta_{H\alpha}^0$, $\eta_{[O II]}^0$, and $\eta_{H\alpha+[N II]}^0$ correspond to the case $\hat{\tau}_V = 0$.

^d 99th percentile range in $|\Delta_m|$ (eq. [19]) obtained when applying the formula to all the models *m* in Table 1 (see text and Fig. 10). For reference, the full (100th percentile) range in $|\Delta_m|$ is indicated in parentheses.

^e H $\alpha+[N II]$ $\lambda\lambda$ 6548, 6583 blend only ($W_{H\alpha+[N II]} > 5 \text{ \AA}$).

patible with ranges of at least a decade in $\eta_{\text{H}\alpha}$ and $\eta_{[\text{O II}]}$. The allowed combinations of ionized-gas parameters alone imply factors of 3.5 and 14 spreads in $\eta_{\text{H}\alpha}$ and $\eta_{[\text{O II}]}$, respectively. We find that, by exploiting the correlations between $\eta_{\text{H}\alpha}$ and $\eta_{[\text{O II}]}$ and various spectral features, we can reduce considerably the uncertainties affecting SFR estimates. For example, with the help of other lines such as [O II], H β , [O III] [N II], or [S II], the uncertainties in SFR estimates based on H α can be reduced to a factor of only 2–3. A similar accuracy can be achieved even if the H α line is blended with the adjacent [N II] lines. Without H α , however, the SFR, the gas-phase oxygen abundance, and the effective absorption optical depth of the dust are difficult to estimate from the [O II], H β , and [O III] lines. The reason for this is that the absorption by dust in the neutral ISM and the ionized-gas parameters are then difficult to constrain independently. This suggests that, while insufficient by itself, the H α line is essential for estimating the star formation rate from the optical emission of a galaxy.

The estimators listed in Table 2 allow one to derive more refined constraints on the star formation rate, the gas-phase oxygen abundance, and the effective absorption optical depth of the dust in galaxies than was previously possible from optical spectra alone. By design, these estimators can be applied directly to observations uncorrected for dust and stellar (H-Balmer) absorption. We can also derive, on demand, the estimators best suited to observational selection criteria other than those exemplified in Table 2. Finally, as shown in §3.2, our full model for the line and continuum emission allows detailed interpretations of whole spectral energy distributions of galaxies in terms of stars, gas, and dust parameters.

ACKNOWLEDGMENTS

We thank M. Fall, G. Ferland, R. Kennicutt, and L. Tresse for valuable discussions. S.C. appreciates the generous hospitality of the MPIA-Garching, and M.L. acknowledges support by the European Commission under TMR grant no. ERBFMBI-CT97-2804. This research was supported in part by the National Science Foundation through grant no. PHY94-07194 to the Institute for Theoretical Physics.

REFERENCES

Allard F., Hauschildt P. H., 1995, ApJ, 445, 433
 Alongi M., Bertelli G., Bressan A., Chiosi C., Fagotto F., Greggio L., Nasi E., 1993, A&AS, 97, 851
 Baldwin J. A., Phillips M. M., Terlevich R., 1981, PASP, 93, 5
 Barbaro G., Poggianti B. M., 1997, A&A, 324, 490
 Bessell M. S., Brett J. M., Scholtz M., Wood P. R., 1989, A&AS, 77, 1
 Bessell M. S., Brett J. M., Scholtz M., Wood P. R., 1991, A&AS, 89, 335
 Binette L., Magris C. G., Stasińska G., Bruzual A. G., 1994, A&A, 292, 13
 Bottorff M., LaMothe J., Momjian E., Verner E., Vinković D., Ferland G., 1998, PASP, 110, 1040
 Bresolin F., Kennicutt R. C., Garnett D. R., 1999, ApJ, 510, 104
 Bressan A., Fagotto F., Bertelli G., Chiosi C., 1993, A&AS, 100, 647
 Bressan A., Chiosi C., Tantalo R., 1996, A&A, 311, 425
 Bruzual A. G., 1983, ApJ, 273, 105
 Bruzual A. G., Charlot S., 1993, ApJ, 405, 538
 Calzetti D., 1997, AJ, 113, 162
 Calzetti D., Kinney A. L., Storchi-Bergmann T., 1994, ApJ, 429, 582
 Campbell A., 1988, ApJ, 335, 644
 Cananzi K., Augarde R., Lequeux J., 1993, A&AS, 101, 599
 Cassinelli J. P., et al., 1995, ApJ, 438, 932
 Charlot S., Fall S. M., 1993, ApJ, 415, 580
 Charlot S., Fall S. M., 2000, ApJ, 539, 718
 Cowie L. L., Songaila A., 1986, ARAA, 24, 499
 Díaz, A. I., Terlevich, E., Vilchez, J. M., Pagel, B. E. J., Edmunds, M. G., 1991, MNRAS, 253, 245
 Draine B. T., Lee H. M., 1984, ApJ, 285, 89
 Evans I. N., Dopita M. A., 1985, ApJS, 58, 125
 Fagotto F., Bressan A., Bertelli G., Chiosi C., 1994a, A&AS, 100, 647
 Fagotto F., Bressan A., Bertelli G., Chiosi C., 1994b, A&AS, 104, 365
 Fagotto F., Bressan A., Bertelli G., Chiosi C., 1994c, A&AS, 105, 29
 Fanelli M. N., O'Connell R. W., Thuan T. X., 1988, ApJ, 334, 665
 Ferguson A. M. N., Wyse R. F. G., Gallagher J. S., Hunter D. A., 1996, AJ 111, 2265
 Ferland G., 1996, Hazy, A Brief Introduction to Cloudy. Internal Report, Univ. Kentucky, USA
 Fluks M. A., Plez B., The P. S., de Winter D., Westerlund B. E., Steenman H.C., 1994, A&AS, 105, 311
 Garnett D. R., Dufour R. J., Peimbert M., Torres-Peimbert S., Shields G. A., Skillman E. D., Terlevich E., Terlevich, R. J., 1995, ApJ, 449L, 77
 Girardi L., Bressan A., Chiosi C., Bertelli G., Nasi E., 1996, A&AS, 117, 113
 Gallagher J. S., Hunter D. A., Bushouse H., 1989, AJ, 97, 700
 García-Vargas M. L., Bressan A., Díaz A. I., 1995, A&AS, 112, 35
 Giallongo E., Fontana A., Madau P., 1997, MNRAS, 289, 629
 González-Delgado, R.M., Leitherer, C., 1999, ApJS, 125, 479
 Grevesse N., Anders E., 1989, in Waddington C.J., ed., Proc AIP Conference 183, Cosmic abundances of matter. New York, p. 1
 Grevesse N., Noel A., 1993, in Prantzos N., Vangioni-Flam E., Casse M., eds, Origin & Evolution of the Elements. Cambridge Univ. Press, p. 15
 Henry R. B. C., Worthey G., 1999, PASP, 111, 919
 Hummer D. G., Mihalas D., 1970, MNRAS, 147, 339
 Hummer D. G., Storey P., 1992, MNRAS, 254, 277
 Hoopes C. G., Walterbos R. A. M., Greenwalt B. E., 1996, AJ, 112, 1429
 Hunter D. A., Gallagher J. S., 1990, ApJ, 362, 480
 Izotov Y. I., Thuan T. X., Lipovetzky V. A., 1994, ApJ, 435, 647
 Jenkins E. B., 1987, in Hollenbach D., Thronson H., eds, Interstellar Processes. Reidel, Dordrecht, p. 533
 Kennicutt R. C., 1983, ApJ, 272, 54
 Kennicutt R. C., 1984, ApJ, 287, 116
 Kennicutt R. C., 1992a, ApJS, 79, 255
 Kennicutt R. C., 1992b, ApJ, 388, 310
 Kennicutt R. C., 1998, ARA&A, 36, 189
 Kennicutt R. C., Tamblyn P., Congdon C. E., 1994, ApJ, 435, 22
 Kinney A. L., Bohlin R. C., Calzetti D., Panagia N., Wyse R. F. G., 1993, ApJS, 86, 5
 Kobulnicky H. A., Kennicutt R.C., Pizagno J.L. 1999, ApJ, 514, 544
 Kurucz R. L., 1992, in Barbuy B., Renzini A., eds, Proc. IAU Symp. 149, The Stellar Populations of Galaxies. Kluwer, Dordrecht, p. 225
 Kurucz R. L., 1995, private communication to T. Lejeune

Leitherer C., Heckman T. M., 1995, ApJS, 96, 9
 Leitherer C., Ferguson H. C., Heckman T. M., Lowenthal J. D.
 1995, ApJ, 454L, 19
 Lehnert M. D., Heckman T. M., 1994, ApJ, 426, 27
 Lejeune T., Cuisinier F., Buser R., 1997, A&AS, 125, 229
 Lejeune T., Cuisinier F., Buser R., 1998, A&AS, 130, 65
 Martin C. L., 1997, ApJ, 491, 561
 Martin P. G., Rouleau F., 1989, in Malina R. F., Bowyer S., eds,
 Extreme Ultraviolet Astronomy. Pergamon, Elmsford, NY, p.
 34
 McCall M. L., Rybski P. M., Shields G. A., 1985, ApJS, 57, 1
 McGaugh S. S., 1991, ApJ, 380, 140
 McQuade K., Calzetti D., Kinney A. L., 1995, ApJS, 97, 331
 Mathis S. J., 1986a, PASP, 98, 995
 Mathis S. J., 1986b, ApJ, 301, 423
 Meurer G. R., Heckman T. M., Calzetti D., 1999, ApJ, 521, 64
 Oey M. S., Kennicutt R. C., 1993, ApJ, 411, 137
 Oey M. S., Kennicutt R. C., 1997, MNRAS, 291, 827
 Osterbrock D. E., 1989, Astrophysics of Gaseous Nebulae and
 Active Galactic Nuclei. Mill Valley: University Science Books
 Scalo, J.M., 1986, FCPh, 11, 1
 Schaerer D., de Koter A., 1997, A&A, 322, 598
 Shields J. C., Kennicutt R. C., 1995, ApJ, 454, 807
 Shields G. A., Searle L., 1978, ApJ, 222, 821
 Snow T. P., Witt A. N., 1996, ApJ, 468L, 65
 Spitzer L., 1978, Physical Processes in the Interstellar Medium.
 Wiley, New York, p. 333
 Stasińska G., 1980, A&A, 85, 359
 Stasińska G., 1990, A&AS, 83, 501
 Stasińska G., Leitherer C., 1996, ApJS, 107, 661
 Storchi-Bergmann T., Kinney A.L., Challis P., 1995, ApJS, 98,
 103
 Terlevich R., Melnick J., Masegosa M., Moles M., Copetti V.F.,
 1991, A&AS, 91, 285
 Tresse L., Rola C., Hammer F., Stasińska G., Le Fevre O., Lilly
 S. J., Crampton D., 1996, MNRAS, 281, 847
 Vacca W. D., 1994, ApJ, 421, 140
 Vacca W. D., Garmany C. D., Shull J. M., 1996, ApJ, 460, 914
 Vila-Costas, M. B., Edmunds M. G., 1993, MNRAS, 265, 199
 Wang J., Heckman T. M., Lehnert M. D., 1997, ApJ, 491, 114
 Worthey G., Faber S. M., Gonzalez J. J., Burstein D., 1994, ApJS,
 94, 687
 Zaritsky D., Kennicutt R. C., Huchra J. P., 1994, ApJ, 420, 87

This paper has been produced using the Royal Astronomical Society/Blackwell Science L^AT_EX style file.